Targeting bias in algorithm optimization improves reconstructions of surface ocean pCO_2

Thea H. Heimdal[1], Abby P. Shaum[1], Viviana Acquaviva[2,1], Amanda R. Fay[1], Devan Samant[1], Julius Busecke[1] & Galen A. McKinley[1]

[1]Columbia University and Lamont-Doherty Earth Observatory, Palisades, NY, USA

[2]New York City College of Technology, City University of New York, Brooklyn, NY, USA

Correspondence to: Thea H. Heimdal (theimdal@ldeo.columbia.edu)

This manuscript is a non-peer reviewed preprint submitted to EarthArXiv. This manuscript has been submitted for publication in Machine Learning:Earth, and is currently undergoing peer-review.

Abstract

In order to fully understand current and future climate impacts from rising carbon emissions, it is crucial to accurately quantify the air-sea CO_2 flux and the ocean carbon sink in space and time. Air-sea flux estimates from observation-based data products used in the Global Carbon Budget show a large spread, and suggest a stronger carbon sink than global ocean biogeochemistry models (GOBMs) in the last decade. Output from GOBMs and Earth system models (ESMs) can be used as 'testbeds' to better understand current estimates of ocean carbon uptake in time and space through sub-sampling experiments. Recent testbed studies show improvement in reconstruction skill with increasing observational coverage, but the direction (over- vs. underestimation) and magnitude of bias for ocean carbon uptake vary significantly. Here, we use a collection of CMIP6 ESMs as a testbed to better understand the causes of the spread of sink estimates in observation-based products. Specifically, we assess how the choice of hyperparameters for the machine learning algorithm and the testbed structure impact reconstruction skill of surface ocean pCO_2 ($spCO_2$) using the pCO_2-Residual method. We find that, when negative mean squared error (nMSE) is used as error metric during hyperparameter optimization, the reconstruction significantly underestimates $spCO_2$ over 2017-2022, irrespective of which CMIP6 ESM is used as a testbed; this results in an overestimation of the global ocean sink, assessed through comparison to the 'testbed truth'. If hyperparameters are selected based on bias as the error metric, this trend of increasingly negative bias is eliminated. When applied to real-world SOCAT data, this leads to

a significantly weaker global ocean carbon sink in 2021-2022 (up to ~ 0.5 Pg C/yr), and less divergence from GOBM estimates. This suggests that the increasingly stronger sink showed by the pCO_2-Residual method in recent years might not represent a real trend, but may be due to algorithmic design choices in the context of sparse and biased observational coverage.

1 Introduction

Observation-based data products estimate full-coverage surface ocean pCO_2 ($spCO_2$) across space and time by extrapolating from sparse $spCO_2$ observations (e.g., Landschützer et al., 2014; Rödenbeck et al., 2015; Gloege et al., 2022; Bennington et al., 2022a,b) using machine learning (ML) and other statistical approaches. These data products utilize the Surface Ocean CO_2 ATlas (SOCAT; Bakker et al., 2016), the largest global database of surface ocean fCO_2 (fugacity of CO_2) observations, from which $spCO_2$ can be derived. Since 1957, more than 33 million high-quality (uncertainty of < 5 μatm) measurements of fCO_2 have been collected, mostly from research vessels and cargo ships, but in recent years, observations from uncrewed surface vehicles have also been included (Sutton et al., 2021; Bakker et al., 2023). Due to a combination of factors, such as limited resources for ocean observing, and the immense size of the global ocean including inaccessible and unsafe regions for research vessels, the SOCAT database represents only about 2 % of the global ocean at monthly 1°x1° spatial resolution over the period of 1982-2022. In addition, the observations are highly biased towards certain regions, especially the northern hemisphere. For example, the Southern Ocean, which is responsible for ~ 40% of the global ocean uptake of anthropogenic CO_2 (Khatiwala et al., 2009), has significant data gaps, particularly in winter months.

All observation-based products rely on the SOCAT database to estimate full coverage $spCO_2$, and there is strong agreement that data sparsity represents a fundamental limitation in the robustness of the results, contributing to significant uncertainties in air-sea CO_2 flux and ocean sink estimates (e.g., Bushinsky et al., 2019; Gregor et al., 2019; Gloege et al., 2021; Mackay et al., 2022; Hauck et al., 2023; Landschützer et al., 2023; Dong et al., 2024a,b; Heimdal et al., 2024; Jersild & Landschützer, 2024; Zhong et al., 2024). Especially, the observation-based products have limited ability to reconstruct $spCO_2$ in certain regions, such as the Southern Ocean, and for interannual to decadal variability (Gloege et al., 2021; Hauck et al., 2023). Air-sea flux estimates from observation-based products, including those used in the Global Carbon Budget (GCB), show an increasing divergence over time from those of global ocean biogeochemistry models (GOBMs) over the last decade (Friedlingstein et al., 2023); observation-based products estimate an increasingly stronger global ocean sink compared to the GOBMs. An important question remains; does the increase in the carbon uptake reflect real changes in the ocean, or is this a consequence of the observation-based products' inability to accurately reconstruct $spCO_2$? And further, how much of the data products' error is due to sparse SOCAT coverage?

Although there is consensus that sparse and biased SOCAT coverage leads to significant uncertainties in the air-sea CO_2 flux estimates from observation-based products, current studies disagree on whether this leads to an over- or underestimation of the carbon sink. Studies comparing Southern Ocean air-sea CO_2 fluxes derived from observation-based products to aircraft observations (Long et al., 2021) and directly measured fluxes (Dong et al., 2024b) suggest that the products underestimate the ocean sink. This is in agreement with Mackay et al. (2022), arguing that increased winter observational coverage would lead to estimates of stronger Southern Ocean carbon uptake. In contrast, by comparing different algorithm training strategies, Zhong et al. (2024) found that increased winter observations would lead to estimates of a weaker Southern Ocean sink. In agreement with Zhong et al. (2024), Bushinsky et al. (2019) and Behncke et al. (2024) showed that additional observations from floats or sailboats weakens Southern Ocean sink estimates. It is, however, important to note that float-derived $spCO_2$ estimates may be positively biased by at least 4 μatm (Williams et al., 2017; Gray et al., 2018); data from floats or sailboats with this magnitude of bias can significantly degrade $spCO_2$ reconstructions (Behncke et al., 2024; Heimdal & McKinley, 2024).

Recent studies have used output from GOBMs or Earth System Models (ESMs) as 'testbeds' to assess the fidelity of ML reconstructions, by sub-sampling GOBM/ESM output assuming current SOCAT coverage, but also including additional coverage from floats, buoys, sailboats or uncrewed surface vehicles (Bushinsky et al., 2019; Stamell et al., 2020; Denvil-Sommer et al., 2021; Gloege et al., 2021; Djeutchouang et al., 2022; Hauck et al., 2023; Heimdal et al., 2024; Heimdal & McKinley, 2024). In a testbed, the full model field is the correct solution ('testbed truth') against which the reconstruction's fidelity can be evaluated. These sub-sampling studies conclude that additional observations, especially in the Southern Ocean, improve the $spCO_2$ reconstructions, as shown by a reduction in reconstruction bias against the 'testbed truth'.

However, as in the aforementioned studies with real-world observations-based products (Bushinsky et al., 2019; Long et al., 2021; Mackay et al., 2022; Behncke et al., 2024; Dong et al., 2024b; Zhong et al., 2024), the testbed studies do not agree as to the sign and magnitude of reconstruction biases, and consequently, the implications for the real-world ocean sink estimated with observation-based products remain unclear. Previous testbed studies have used different reconstruction methods, sampling masks, testbed models (including both GOBMs and ESMs) and air-sea flux calculations. While there is no doubt that sparse sampling is a fundamental challenge, it remains unclear what can be concluded about the sign and magnitude of reconstruction biases, and the resulting implications for the global carbon budget.

In this study, we quantify how the choice of testbed structure and algorithm hyperparameters impacts the long-term variability of annual bias in reconstructed $spCO_2$ and air-sea CO_2 flux. This is done by sub-sampling from a testbed spanning a large number of ESM structures and internal variabilities, but keeping the reconstruction method and sampling mask (SOCATv2023; Bakker et al., 2023) constant. We use a testbed that includes a total of 45 ensemble members from 9 different CMIP6 ESMs, and reconstruct $spCO_2$ over 1982-2022 using the pCO_2-Residual method (Bennington et al., 2022a). Further, we explore different error metrics as a basis for hyperparameter selection during algorithm optimization. As pointed out by Zhong et al. (2024), a promising path forward, in addition to increasing the observational coverage, would be investigating whether algorithm improvement could reduce bias and errors in pCO_2 reconstructions. Negative mean squared error (nMSE) is traditionally used as the basis for hyperparameter selection, but here we also test the impact of using bias as the error metric that is minimized when choosing hyperparameters. Previous sub-sampling experiments have shown that biases in $spCO_2$ reconstructions significantly impact the long-term trend and variability of the estimated air-sea flux and ocean carbon uptake (Hauck et al., 2023; Heimdal et al., 2024; Heimdal & McKinley, 2024). We explore whether targeting bias during hyperparameter selection could thus potentially reduce reconstruction biases over time and reduce temporal variability in the fidelity of the $spCO_2$ reconstruction.

By using a testbed, we do not aim to predict real-world $spCO_2$ or air-sea CO_2 fluxes. Instead, we assess the accuracy with which the pCO_2-Residual method (Bennington et al., 2022a) can reconstruct the $spCO_2$ 'testbed truth', given inputs of samples consistent with real-world

SOCAT coverage. The utility of a testbed comes from the fact that the $spCO_2$ field is known precisely at all times and 1°x1° points. When using real-world SOCAT data, the quality of the reconstruction is estimated using only on a subset of the data (the test set; typically 20% of available data), which significantly underrepresent many regions, such as the Southern Ocean. On the other hand, when using a testbed, the $spCO_2$ reconstructed by the ML algorithm can be robustly evaluated in space and time against the 'testbed truth' using all 1°x1° points of the full testbed $spCO_2$ field.

There are additional sources of uncertainties in the ocean carbon sink estimates that are not considered here, such as measurement uncertainty, parameterization of gas exchange transfer velocity (*k*) and wind products in air-sea CO_2 flux calculations, the riverine correction, the cool skin effect, temperature gradients, or the influence of sea ice (e.g., Roobaert et al., 2018; Watson et al., 2020; Fay et al., 2021; Jersild & Landschützer, 2024; Dong et al., 2024b; Nickford et al., 2024). The goal here is to improve our understanding of algorithmic reconstruction skill of the pCO_2-Residual method with current SOCAT coverage; and further, to better understand how hyperparameter tuning impacts reconstruction biases over time.

2 Methods

2.1 The CMIP6 testbed

The CMIP6 testbed presented here is an update from the CMIP5 testbed used in previous sub-sampling studies (Stammel et al., 2020; Gloege et al., 2021; Bennington et al., 2022a; Heimdal et al., 2024; Heimdal & McKinley, 2024). It includes the latest generation of ESMs from the Coupled Model Intercomparison Project (CMIP) (CMIP6; Eyring et al., 2016). With this new testbed compared to the previous CMIP5-based one, we have a greater variety of ESMs (9 vs. 4), thus spanning more ESM structures, which has previously been shown to have an impact on whether the reconstruction over- or underestimates $spCO_2$ (Stammel et al., 2020; Heimdal et al., 2024; Heimdal & McKinley, 2024). This testbed includes a total of 45 members from nine independent CMIP6 ESMs (**Table 1**), selected because they provide output for both surface ocean partial pressure of CO_2 ($spCO_2$) and the driver variables needed for the pCO_2-Residual method. Due to varying availability of $spCO_2$ output for each ESM, the number of members per ESM in our testbed varies (between 1 to 18 ensembles; see **Table 1**). The 45-member testbed includes ESM output from 1982 to 2022, but the testbed can be extended beyond 2022 for future studies, as well as expanded in size, subject to the availability of the needed ESM output.

Each ensemble member has undergone the same forcing; solar, volcanic and historical atmospheric CO_2 through 2015, followed by Representative Concentration Pathway 4.5 (RCP4.5) through 2022. The historical and RCP4.5 atmospheric CO_2 (xCO_2) is used as a driver variable for the ML algorithm (**Table 2**). Different members of the same ESM represent the internal variability of each ESM, i.e., differences in possible ocean-atmosphere states. This has been done by perturbing the initial state of the Earth system at the start of each simulation.

For each ensemble member, $spCO_2$ and associated driver variables (e.g., SST, SSS, Chl-a; **Table 2**) are sampled monthly at a 1°x1° resolution, at times and locations equivalent to real-world SOCAT coverage (SOCATv2023; Bakker et al., 2023). We also calculate interannual anomalies for SST, SSS and Chl-a. This was done by calculating a monthly climatology (e.g., average of all Januarys), and subtracting this from the appropriate month. In addition, time of year and geographic location are calculated using an N-vector transformation of latitude and longitude, and a time transformation of day of year, which replaces these coordinates/dates to continuous values between 0 and 1. Following Heimdal et al. (2024), testbed output for coastal areas, the Arctic Ocean (>79°N) and marginal seas (Hudson Bay, Caspian Sea, Black Sea, Mediterranean Sea, Baltic Sea, Java Sea, Red Sea and Sea of Okhotsk) were removed prior to algorithm processing.

Table 1: Earth System Models (ESMs) and number of members in the CMIP6 testbed.

ESM name	# of members
UKESM1-0-LL	5
ACCESS-ESM1-5	2
CMCC-ESM2	1
CESM2-WACCM	3
CESM2	3
CanESM5-CanOE	3
CanESM5	18
MPI-ESM1-2-LR	9
GFDL-ESM4	1

Table 2: Target and driver variables, and processing steps.

	Variable		Description/processing
Target	**$spCO_2$-Residual**	$spCO_2$ - $spCO_2$-T	See Section 2.2
Drivers	**SST**	Sea surface temperature	Monthly SST
	SSS	Sea surface salinity	Monthly SSS
	MLD	Mixed Layer Depth	Log of MLD
	Chl-a	Chlorophyll-a	Log of Chl-a
	Chl-a anomaly	Interannual anomaly	Monthly Chl-a - monthly climatology
	SST anomaly	Interannual anomaly	Monthly SST - monthly climatology
	SSS anomaly	Interannual anomaly	Monthly SSS - monthly climatology
	xCO_2	Atmospheric pCO_2	Historical values through 2015, RCP 4.5 through 2022
	A	Geographic location	$\sin(\boldsymbol{\lambda})$
	B	Geographic location	$\sin(\boldsymbol{\mu}) \cos(\lambda)$
	C	Geographic location	$(-\cos(\boldsymbol{\mu}) \cos(\boldsymbol{\lambda}))$
	T0	Time of year	cos(day of year*2$\boldsymbol{\pi}$/365)
	T1	Time of year	sin(day of year*2$\boldsymbol{\pi}$/365)

2.2 The pCO_2-Residual method

The pCO_2-Residual method (Bennington et al., 2022a) was used to reconstruct $spCO_2$ in space and time. A brief description is provided below, but for further details see Bennington et al. (2022a). Prior to algorithm processing, the direct effect of temperature on $spCO_2$ is removed. This temperature-driven component ($spCO_2$-T) is calculated using the equation of Takahashi et al. (2002):

$$spCO_2\text{-T} = spCO_2^{mean} * \exp[0.0423 * (SST\text{-}SST^{mean})]$$

where $spCO_2^{mean}$ and SST^{mean} are the long-term means of $spCO_2$ and temperature, respectively, using all 1°x1° grid cells from the testbed. The $spCO_2$-Residual is calculated by subtracting $spCO_2$-T from $spCO_2$. Following Heimdal et al. (2024), $spCO_2$-Residual values ranging between > 250 μatm and < -250 μatm were removed as they are unlikely to represent physical conditions in the real ocean. The excluded data points represent less than 0.1 % per ESM, and mostly occur in output from GFDL and CMCC.

The eXtreme Gradient Boosting method (XGB; Chen & Guestrin, 2016) is then used to develop a model that predicts the target variable ($spCO_2$-Residual) from the driver variables (**Table 2**). The driver variables are proxies for processes influencing $spCO_2$. Full-coverage driver variable datasets are processed through the algorithm to produce global full-coverage $spCO_2$-Residuals. For the final reconstruction of $spCO_2$ across all space and time points, the previously calculated

$spCO_2$-T values are added back to the reconstructed $spCO_2$-Residual values. The full XGB process is repeated individually for each of the 45 CMIP6 testbed members, providing a total of 45 reconstructions.

2.3 Reconstruction error metrics

To build the predictive ML model, the $spCO_2$-Residual and associated driver variables are split into training, validation, and testing sets. The test and validation set each account for 20% of the data, leaving 60% for training. The training set is used to learn the relationship between the driver variables and target, or more concretely, to construct the decision trees that are the building blocks of XGB. The validation set is used to optimize the algorithm hyperparameters, which define the architecture of decision trees used in the model, as well as the procedure used in creating ensembles of trees. Finally, the test set is used to evaluate the performance of the reconstruction on unseen data, by statistically comparing the reconstruction and the ESMs $spCO_2$ fields ('testbed truth'). When using real-world data, it is only possible to statistically compare the reconstruction to the test set. Since we are using a testbed, here, we calculate reconstruction error statistics for the 'full' CMIP6 testbed ESM fields (i.e., all 1°x1° grid cells, not only those representing the test set, but excluding those used for training).

Here, we focus on bias and root-mean-squared error (RMSE) as reconstruction error metrics. Reconstruction bias, which is a measure of whether the reconstruction overestimates (positive bias) or underestimates (negative bias) $spCO_2$, is calculated as:

$$bias = \overline{reconstruction} - \overline{testbed\ truth}$$

RMSE is calculated as:

$$\text{RMSE} = \sqrt{\overline{(reconstruction - testbed\ truth)^2}}$$

where, unless otherwise specified, the overbar indicates a mean across all 1°x1° grid cells globally and all months over the period of 1982-2022 or 2017-2022. Global mean reconstruction bias and RMSE is first calculated for each individual member of the testbed. For ESMs with more than one member (**Table 1**), an 'ESM mean' was calculated, which represents an average of bias or RMSE for all individual members of their respective ESM. The 'testbed mean' represents a mean of the nine ESM means.

2.4 Identifying hyperparameters

The validation set (**Sect. 2.3**) is used to optimize the algorithm hyperparameters. We perform a grid search consisting of 64 possible combinations of hyperparameters, including four different learning rates, depth levels, and numbers of decision trees (**Table 3**). These parameters span a wide range of possible model behavior and represent, respectively, the amplitude of the contribution of each additional tree to the final model, the complexity of the decision trees used as base estimators, and the total number of decision trees (equivalently, the number of boosting iterations) in the final model. The grid search is performed on one member per ESM, and each combination of hyperparameters is applied three times (k-fold cross-validation). After performing a grid search on one member per ESM (nine in total), the combination of hyperparameters that led to the lowest error metric value (i.e., the "best" ML model) is chosen and then applied to the remaining members for that respective ESM. We test the impact of choosing either negative mean squared error (nMSE) (nMSE_run) or bias (Bias_run) as the error metric of the grid search. This leads to a total of 18 grid searches (nine nMSE_runs and nine Bias_runs), with 64 hyperparameter combinations in each. It is important to note the difference between 'hyperparameter error metrics' (here, bias and nMSE) and 'reconstruction error metrics' (here, bias and RMSE; **Sect. 2.3**). The 'reconstruction error metrics' evaluate the performance of the final full reconstruction to the 'testbed truth' (see **Sect. 2.3**). The 'hyperparameter error metrics' evaluate the impact of the hyperparameters used in the ML model.

Table 3: Hyperparameters used in the grid search during algorithm optimization; a total of 64 possible combinations.

Max depth	Learning rate	Decision trees
6	0.05	500
7	0.1	1000
10	0.3	2000
15	0.4	4000

2.5 Air-sea CO_2 flux

In order to assess the implications of algorithm optimization on the quantification of real-world air-sea CO_2 fluxes and ocean carbon uptake, we use the pCO_2-Residual method to reconstruct fCO_2 using real-world SOCAT observations (SOCATv2023; Bakker et al., 2023). We use the pCO_2-Residual method as presented in Bennington et al. (2022a), but apply a combination of optimized hyperparameters found in this study (i.e., maximum depth level: 6; learning rate: 0.3; decision trees: 4,000; see **Sect. 4.2**). We compare this reconstruction to the original pCO_2-Residual reconstruction method from Bennington et al. (2022a), where nMSE was used as the hyperparameter error metric during algorithm optimization (maximum depth level: 9; learning rate: 0.3; decision trees: 1,000; Bennington et al., 2022a). Air-sea CO_2 fluxes are calculated using the bulk formulation with python package Seaflux.1.3.1 (https://github.com/lukegre/SeaFlux; Gregor et al. 2021; Fay et al., 2021):

$$\text{Flux} = k_w \cdot \text{sol} \cdot (fCO_2^{ocn} - fCO_2^{atm}) \cdot (1 - \text{ice})$$

where 'k_w' is the gas transfer velocity, 'sol' is the solubility of CO_2 in seawater (in units of mol m^{-3} μatm^{-1}), 'fCO_2^{ocn}' is the fugacity of surface ocean carbon (in μatm), and fCO_2^{atm} (in μatm) is the fugacity of atmospheric CO_2 in the marine boundary layer. To account for the seasonal ice cover in high latitudes, the fluxes were weighted by 1 minus the ice fraction ('ice'), i.e., the open ocean fraction. Inputs to the calculation include EN4.2.2 salinity (Good et al., 2013), SST and ice fraction from NOAA Optimum Interpolation Sea Surface Temperature V2 (OISSTv2) (Reynolds et al., 2002), and three surface winds and associated wind scaling factors from the European Centre for Medium-Range Weather Forecasts (ECMWF ERA5; Hersbach et al., 2020), Cross-Calibrated Multi-Platform v2 (CCMP2; Atlas et al., 2011) and Japanese 55-year Reanalysis (JRA-55; Kobayashi et al., 2015).

We compare the air-sea CO_2 fluxes calculated from the two pCO_2-Residual reconstructions (using original and optimized hyperparameters) to those from GOBMs and observation-based products presented in the 2023 GCB (Friendlingstein et al., 2023). All observation-based product fluxes were adjusted assuming a riverine carbon flux of 0.65 Gt C/yr following Friedlingstein et al. (2023) in order to compare with GOBM fluxes.

3 Results

3.1 Algorithm hyperparameters

The combination of hyperparameters that led to the lowest mean 1982-2022 nMSE value were identical for seven out of nine nMSE_runs, with 4,000 decision trees, a maximum depth of 10, and a learning rate of 0.05 (**Table 4**). For CanESM5 and CanESM5-CanOE, however, a maximum depth of 7, and a learning rate of 0.1 was chosen instead. For the nine Bias_runs, very different combinations of hyperparameters were chosen for each ESM sub-sampled (**Table 4**). None of the Bias_runs show the same set of hyperparameters, which vary between 6, 7 or 10 maximum depth levels, a learning rate of 0.1, 0.3 or 0.4, and 500, 1,000, 2,000 or 4,000 decision trees. For CanESM5, both the nMSE_run and Bias_run chose the same hyperparameters.

In general, it is expected that different combinations of parameters may result in similar performances; for example, in XGBoost, a higher number of boosting rounds can be compensated by a smaller learning rate (e.g., Acquaviva, 2023). To estimate the impact of hyperparameter selection on the optimization process, we compare the disparity in scores for the various ML models to the typical variation in the test scores arising from sample variance (the effect of choosing different partitions of the data for training, validation, and test) through the standard deviation of the three scores in the k-fold cross-validation process. For the nMSE_Run, for each ESM sub-sampled, only one or two combinations of hyperparameters (out of 64 possible) led to a mean 1982-2022 nMSE value within the mean standard deviation of the 64 nMSE scores. The top performing models all had 4,000 decision trees, with a maximum depth of 7 or 10 and a learning rate of 0.05 or 0.1. This indicates that a large number of iterations is crucial to high model skill. In contrast, for the Bias_run, the impact of specific hyperparameter choices is less clear. The number of combinations that led to a mean 1982-2022 bias value within the mean standard deviation of the 64 bias scores is much larger, and varies significantly between the different ESM sub-sampled, from 10 to 62 out of the 64 possible combinations. It is important to note that, over a large time period such as 1982-2022, large positive and negative biases may be averaging, leading to mean bias values near zero. Thus, while the mean biases shown for the different combinations may be similar, the different combinations of hyperparameters result in different reconstruction results over time (**Fig. 1**).

Table 4: Hyperparameters chosen for the different Earth System Models (ESMs) in the CMIP6 testbed, when negative mean squared error (nMSE_run) and bias (Bias_run) were the basis of error metrics for hyperparameter selection during algorithm optimization.

	nMSE_run | Bias_run		
ESM name	**Max Depth**	**Learning rate**	**Decision trees**
UKESM1-0-LL	10|10	0.05 | 0.1	4000 | 4000
ACCESS-ESM1-5	10| 6	0.05 | 0.4	4000 | 4000
CMCC-ESM2	10|10	0.05 | 0.4	4000 | 1000
CESM2-WACCM	10| 6	0.05 | 0.3	4000 | 4000
CESM2	10| 6	0.05 | 0.1	4000 | 2000
CanESM5-CanOE	7 | 6	0.1 | 0.3	4000 | 500
CanESM5	7 | 7	0.1 | 0.1	4000 | 4000
MPI-ESM1-2-LR	10| 6	0.05 | 0.4	4000 | 500
GFDL-ESM4	10| 6	0.05 | 0.4	4000 | 2000

3.2 Reconstruction error metrics

3.2.1 Reconstruction bias

All runs overestimate $spCO_2$ in the 1980s (> 2 µatm), before reconstruction bias steadily decrease towards zero until the early 1990s, and then straddle generally between ± 1 µatm (**Fig. 1**). For the nMSE_runs (pink lines; **Fig. 1**), a trend of increasingly negative bias values ($spCO_2$ is underestimated) occurs towards the end of the testbed period, generally from around 2017 and onwards. Most ensemble members and the mean for each ESM have a growing negative bias for all ESMs. For the period of 2017-2022, ESM mean reconstruction biases for the nMSE_runs range from -1.5 µatm to -0.01 µatm (**Table 5**).

When pCO_2-Residual hyperparameters are set with bias as the grid search criteria (Bias_runs), the reconstruction is less likely to underestimate $spCO_2$ in 2017-2022, or to overestimate in the 1980s (blue lines; **Fig. 1**). For most of the ESMs, the Bias_runs show near-zero or positive mean reconstruction biases over 2017-2022 (between 0.08 µatm and 0.4 µatm; **Table 5**). For four ESMs however (i.e., CMCC, CanESM5, MPI and UKESM1), negative reconstruction biases after 2017 are found (between -1.3 µatm and -0.3 µatm; **Table 5**). Averaging over all 45 members of the testbed, the 2017-2022 global 'testbed mean' reconstruction bias for the Bias_run is -0.2 µatm, notably smaller than for the nMSE_run (-0.6 µatm; **Table 5**).

3.2.2 Reconstruction Root-mean squared error (RMSE)

For all runs, reconstruction RMSE is highest in the first and last years of the analysis period (**Fig. 2**), indicating reduced reconstruction skill for generalization in the earliest and latest years of the reconstruction. The nMSE_runs sub-sampling CMCC, CanESM5-CanOE and MPI show consistently lower RMSEs over the whole testbed period compared to the Bias_runs. For the remaining ESMs, both sets have similar RMSEs over 1982-2022 (**Fig. 2**). For 2017-2022, the mean across each ESM ranges from 8.8 µatm to 12.9 µatm for the nMSE_runs, and 8.4 µatm to 13.6 µatm for the Bias_runs (**Table 5**). Only the reconstruction using one member of CMCC shows a significant increase (1.7 µatm; **Table 5**) in the 2017-2022 RMSE when bias is used to define the hyperparameters. Averaging over all 45 members of the testbed, the 2017-2022 global 'testbed mean' reconstruction RMSE for the nMSE_run (10.2 µatm) and Bias_run (10.5 µatm) are very similar (**Table 5**).

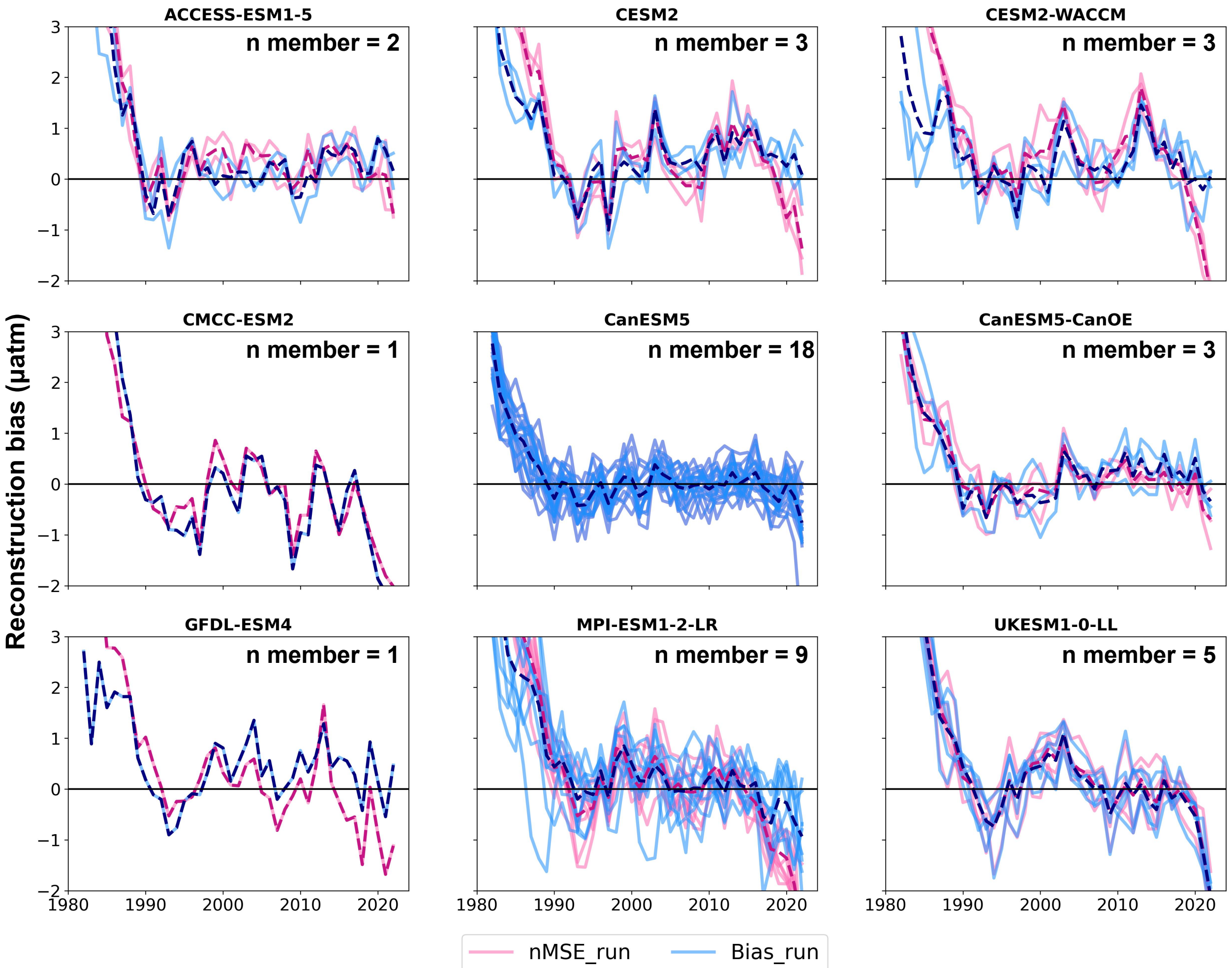

Figure 1: Annual global mean reconstruction bias for the 45 reconstructions of the testbed, grouped by ESM (Table 1). nMSE_run (pink) = hyperparameters were chosen based on negative mean squared error (nMSE) as error metric. Bias_run (blue) = hyperparameters were chosen based on bias as the error metric. CanESM5 has the same optimal hyperparameters in both cases, so the reconstructions are identical (Table 4). Bold dashed lines for each color suite are ESM means.

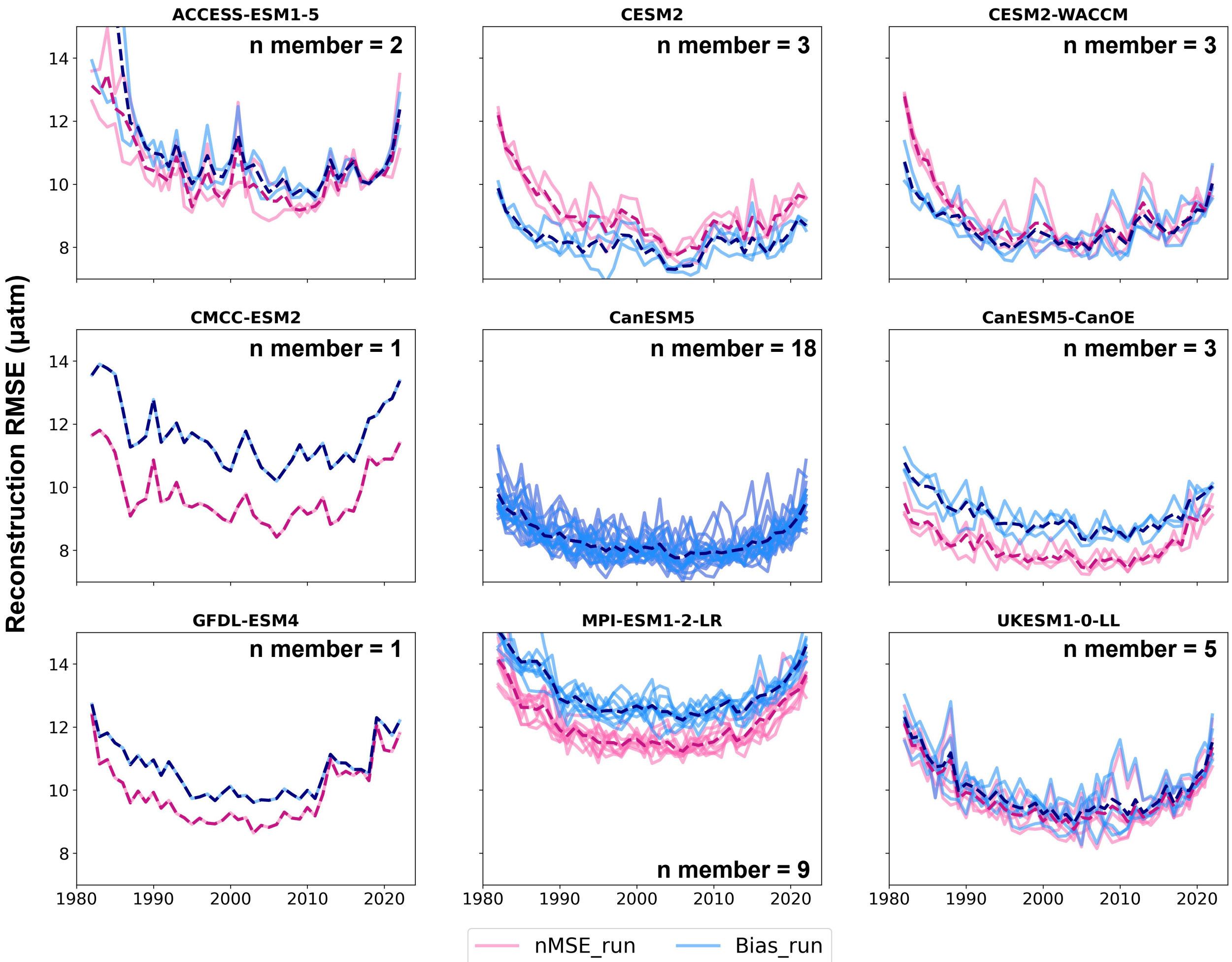

Figure 2: Annual global mean reconstruction root-mean squared error (RMSE) for the 45 reconstructions of the testbed. nMSE_run (pink) = hyperparameters were chosen based on negative mean squared error (nMSE) as error metric. Bias_run (blue) = hyperparameters were chosen based on bias as the error metric. CanESM5 has the same optimal hyperparameters in both cases, so the reconstructions are identical (Table 4). Bold dashed lines for each color suite are ESM means.

Table 5: Global 2017-2022 mean reconstruction bias and RMSE for individual ESMs and the 'testbed mean' (45 members) for the nMSE_run and Bias_run.

ESM name (# of members)	nMSE_run | Bias_run BIAS	RMSE
UKESM1-0-LL (5)	-0.7 | -0.7	10.2 | 10.4
ACCESS-ESM1-5 (2)	-0.01 | 0.4	10.7 | 10.7
CMCC-ESM2 (1)	-1.1 | -1.3	10.8 | 12.5
CESM2-WACCM (3)	-0.7 | 0.08	9.2 | 9.1
CESM2 (3)	-0.4 | 0.4	9.2 | 8.4
CanESM5-CanOE (3)	-0.2 | 0.08	8.9 | 9.5
CanESM5 (18)	-0.3 | -0.3	8.8 | 8.8
MPI-ESM1-2-LR (9)	-1.5 | -0.5	12.9 | 13.6
GFDL-ESM4 (1)	-0.9 | 0.1	11.2 | 11.6
Testbed mean	**-0.6 | -0.2**	**10.2 | 10.5**

4 Discussion

4.1 The negative trend in reconstruction bias over 2017-2022

When using nMSE as error metric during algorithm optimization, we show that the resulting reconstruction significantly overestimates $spCO_2$ is in the 1980s, and underestimates $spCO_2$ for 2017 through 2022 (**Fig. 1**). This pattern cannot be attributed to the ESM field used as the testbed, as all members show the same trends, though with variable magnitude (**Fig. 1**; **Table 5**). These biases are accompanied by high reconstruction RMSEs indicating reduced reconstruction skill for generalization in the earliest and latest years of the reconstruction (**Fig. 2**). Reconstruction biases directly impact the estimated air-sea CO_2 flux. The CO_2 flux between the ocean and atmosphere can be described as: $\Delta pCO_2 = pCO_2^{ocean} - pCO_2^{atm}$. Low pCO_2^{ocean} leads to a negative ΔpCO_2 ($pCO_2^{ocean} - pCO_2^{atm}$), which indicates carbon uptake as opposed to outgassing. The 2017-2022 negative reconstruction bias shown by our nMSE_Run means that pCO_2^{ocean} is underestimated compared to the 'testbed truth'. Since the reconstructed pCO_2^{ocean} is lower than the 'testbed truth', this means that our reconstruction overestimates the carbon uptake.

The trend of negative reconstruction bias over 2017-2022 shown by our experiments matches the pattern of an increasingly stronger global ocean sink and deviation from the GOBMs in the last decade, as estimated by both the pCO_2-Residual method (Bennington et al., 2022a) and the GCB observation-based products (Friedlingstein et al., 2023). The trend of high reconstruction bias and errors at the beginning and end of the testbed period also matches the distribution of SOCAT observations; they are notably scarce from 1982 until the mid-1990s, before a steady increase occurs with a peak in 2017, followed by a decrease in 2017-2022 (**Fig. S1**). Is the trend of increasingly negative 2017-2022 reconstruction bias, and increase in the ocean carbon sink, a result of declining SOCAT coverage since 2017? To test this, we randomly shuffled the years of SOCAT observations five times and reconstructed $spCO_2$ using the same hyperparameters as the nMSE_run (see **Sect. S1** in **Supplement** for details). For all five shuffled runs, the reconstructions significantly improve in the 1980s, but the negative reconstruction bias towards the end of the testbed period remains, albeit with different magnitudes (**Fig. 3**). We find no correlation between the magnitude of reconstruction bias and number of SOCAT observations in a particular year (**Fig. S2**). This suggests that the recent decline in SOCAT coverage alone is not responsible for the trend of increasingly negative reconstruction biases after 2017.

The long-term positive trend in $spCO_2$ since the 1980s has the potential to impact the ability of algorithms to represent the data (Gloege et al., 2021). A foundational assumption of ML is that data are normally distributed and that the data to be reconstructed are distributed to the training set. Thus, with $spCO_2$ as the target variable, which increases with time, the algorithm must predict a right-skewed data distribution. The mean $spCO_2$ of the full 'testbed truth' (all 1°x1° grid cells) is 356 μatm, occurring in the year 2002. This means that the mean $spCO_2$ is far away from the "extremes" in each end, with comparably low $spCO_2$ in the 1980s and high $spCO_2$ in the 2020s. This effect likely contributes to reconstruction overestimation of $spCO_2$ in the 1980s and underestimation in the 2020s. Shuffling the SOCAT years reduces the very high reconstruction biases in the 1980s (> 2 μatm), which likely is due both to the increased sampling and the mean of the training distribution falling now more centrally in the reconstruction period (**Fig. S1**).

When using bias as error metric instead of nMSE, for several of the ESMs sub-sampled, the trend of negative bias in 2017-2022 disappears, or is significantly dampened (**Fig. 1**; **Table 5**). This suggests that it is possible to counteract some of the negative impact of the right-skewed $spCO_2$ data distribution, by targeting bias in the algorithm optimization process.

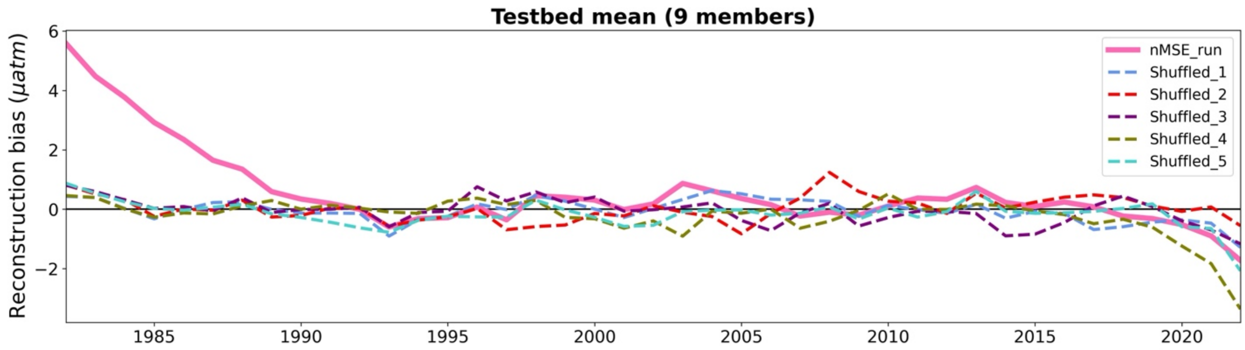

Figure 3: Annual global 'testbed mean' (one member per ESM, 9 in total) reconstruction bias for the nMSE_run and the five shuffled runs.

4.2 Experimental run with optimized hyperparameters

Some of the reconstructions, particularly those sub-sampling UKESM1, CMCC and MPI, still underestimate $spCO_2$ with bias as the hyperparameter error metric (**Fig. 1**; **Table 5)**, leading to a negative 2017-2022 'testbed mean' reconstruction bias of -0.2 µatm (**Table 5**). To explore if it is possible to further improve reconstruction bias, we performed an additional run (Optimized_run) applying the combination of hyperparameters that led to reconstruction biases closest to zero throughout the whole testbed period, which is the Bias_run sub-sampling CESM2-WACCM (**Fig. 1**; **Table 5**). These optimized hyperparameters were applied to all 45 members of the testbed (maximum depth level: 6; learning rate: 0.3; decision trees: 4,000 decision trees; **Table 4**).

In the main text, we discuss only the 'testbed mean' reconstruction bias. A description of the ensemble spread and comparisons between ESMs for the Optimized_run can be found in **Sect. S2** in the **Supplement** and are shown in **Figs. S3**, **S4**. With optimized hyperparameters applied to all ESMs in the testbed, negative reconstruction biases after 2017 disappears (**Fig. 4**); the 2017-2022 'testbed mean' bias is zero (**Table S1**). Overestimation of $spCO_2$ in the 1980s is also reduced (**Fig. 4**). This suggests that the optimized hyperparameters lead to an improved reconstruction globally.

Improvements due to the optimized hyperparameters generally occur in the 1980s globally, and in the Southern Hemisphere, especially in the last few years of the testbed period (**Fig. S5**). The negative bias shown throughout the Southern Ocean by the nMSE_Run is dampened in the Optimized_run, but some areas show positive biases instead (**Fig. S6**). This suggests that, when applying the optimized hyperparameters, regional positive and negative biases are averaging, leading to a global 2017-2022 ‘testbed mean’ of zero.

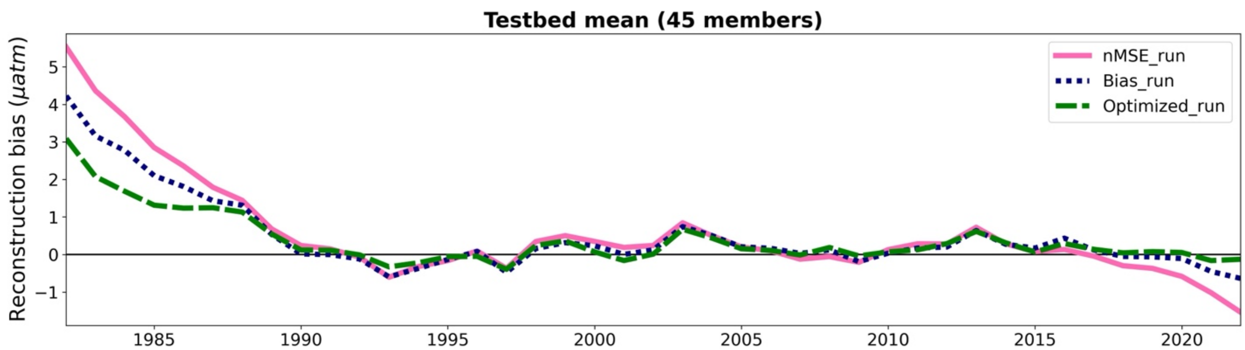

Figure 4: Annual global mean reconstruction bias averaged over the 45 members of the testbed (‘testbed mean’). nMSE_run (pink solid) = hyperparameters were chosen based on negative mean squared error (nMSE) as error metric. Bias_run (blue dotted) = hyperparameters were chosen based on bias as error metric. Optimized_run (green dashed) = the same set of optimized hyperparameters were applied for all 45 reconstructions.

4.3 Implications for real-world fCO_2 reconstructions and air-sea CO_2 flux

In order to assess the implications of algorithm optimization on the quantification of real-world air-sea CO_2 fluxes and ocean carbon uptake, we used the pCO_2-Residual method to reconstruct fCO_2 using real-world SOCAT observations (SOCATv2023; Bakker et al., 2023). We applied both the optimized hyperparameters from this study, and the original hyperparameters from Bennington et al. (2022a), where nMSE was used as the hyperparameter metric during algorithm optimization (maximum depth level: 9; learning rate: 0.3; decision trees: 1000; Bennington et al., 2022a).

Since we are using real-world SOCAT data for these reconstructions, and not a testbed, we cannot compare the full reconstruction results to a ‘truth’; instead, we must calculate reconstruction error metrics using the test set (see **Sect. 2.3**). The reconstruction using the optimized hyperparameters shows a slightly lower global 1982-2022 mean RMSE (18.8 µatm), mean average error (12.4 µatm) and median average error (8.2 µatm) and higher correlation (0.91), but larger bias (-0.1 µatm) compared to the original reconstruction (19.0 µatm, 12.5 µatm, 8.3 µatm, 0.91 and -0.07 µatm, respectively; **Table 6**).

Given what we have seen using the testbed (**Fig. 1**), mean bias over a large time period such as 1982-2022 is likely not a good measure for comparing skill in this use case, as it is likely that positive biases in the 1980s may be averaging with negative biases in the 2010s and 2020s. We calculated annual mean biases by comparing all available monthly 1°x1° data points in SOCAT with the corresponding reconstructed fCO_2 values. When considering the last ten years only, the optimized reconstruction shows biases closer to zero compared to the original reconstruction (**Fig. 5**). Overall, the test error metrics also show slightly better skill for the optimized reconstruction (**Table 6**), which suggests that the optimized hyperparameters lead to an improved reconstruction not only in the testbed, but also when using real-world SOCAT data.

Using the two SOCAT reconstructions (with optimized and original hyperparameters), we calculate the global air-sea CO_2 flux over the period of 1982-2022 (see **Sect. 2.5**). As shown by **Fig. 6**, when using the optimized hyperparameters in the ML model, the global ocean carbon uptake in 2022 is reduced by as much as ~ 0.5 Pg C/yr, and there is less divergence from the GOBM estimates. This suggests, at least for the pCO_2-Residual method, that the 2022 increase in carbon uptake shown for the original pCO_2-Residual reconstruction is at least partially due to algorithm optimization. Whether algorithm tuning for the GCB observation-based products, which incorporate different ML methods than the tree-based pCO_2-Residual method, would also lead to a reduced carbon sink, should be explored in future studies.

Our results also show that important scientific results that can affect future data campaigns and policy, such as the trend in the ocean carbon sink, may depend significantly on the choice of data, metrics, algorithm, and hyperparameter optimization pipelines. As a result, it is crucial to be explicit about all these choices when reporting the results of ML/AI-based models. This allows, on one hand, a fairer comparison to other results in the literature, and on the other hand, serves to open the proverbial black box of ML/AI-based tools and to make them accessible to more members of the ocean science community, as emphasized by Acquaviva et al. (2024).

Table 6: Test statistics for the optimized and original fCO_2 reconstructions using real-world SOCAT data (SOCATv2023; Bakker et al., 2023). The test statistics represent global means over 1982-2022 and a mean of five runs (see Table S2 for individual run test statistics).

Test error metrics	**Mean 5 runs**
Mean (1982-2022)	Optimized | Original
RMSE (uatm)	18.8 | 19.0
Bias (uatm)	-0.1 | -0.07
Mean AE (uatm)	12.4 | 12.5
Median AE (uatm)	8.2 | 8.3
Correlation	0.91 | 0.90

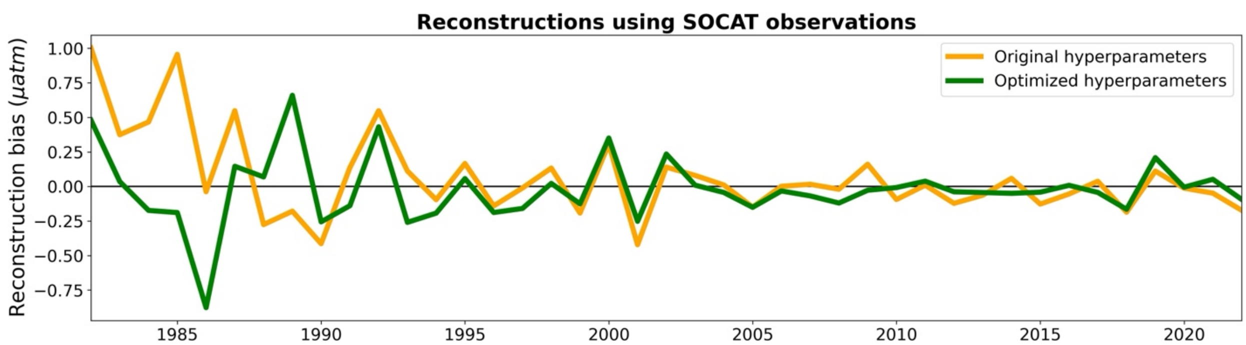

Figure 5: Annual global mean reconstruction bias for fCO_2 reconstructions using real-world SOCAT observations. Original hyperparameters = hyperparameters from Bennington et al. (2022a). Optimized hyperparameters = optimized hyperparameters from this study. Reconstructed fCO_2 is compared to the full SOCAT dataset. Note that the bias calculation includes all data points in SOCAT, including those used for training, so the resulting biases are lower than what would be the case if only the test set were compared.

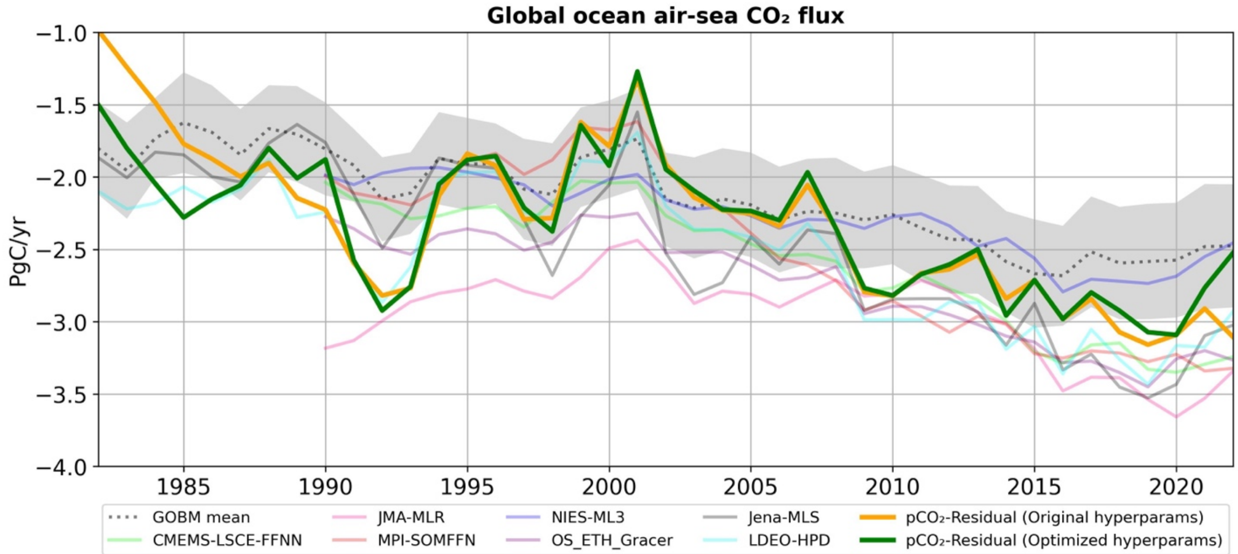

Figure 6: Annual mean global air-sea CO_2 flux for the global ocean biogeochemical models (GOBMs; gray shading: one standard deviation; dotted line is the mean) and observation-based products (solid lines) used in the Global Carbon Budget (Friedlingstein et al., 2023). The bold lines represent the air-sea CO_2 flux estimated by the pCO_2-Residual method using real-world SOCAT observations, with optimized hyperparameters (green) or original hyperparameters (orange) from Bennington et al. (2022a).

4.4 The choice of testbed and its impacts

For all of our experiments, regardless of algorithm optimization, all ESM means show high positive bias in the 1980s, negative bias in the early 1990s, and a sharp positive peak shortly after year 2000 (**Figs. 1**, **S3**). This pattern of reconstruction bias over time is thus not impacted by the ESM model structure, and is likely a result of the ML method, combined with the spatiotemporal resolution of the observations used to train the algorithm. The ESM structure does however impact absolute values of reconstruction bias and RMSE (**Figs. 1**, **2**); for example, the peak of positive bias in the early 2000s is much larger for CESM2 compared to CanESM5, and while all ensembles show a negative bias in 2022 for the nMSE_Run, the magnitude differs significantly (**Fig. 1**). Further, the ensemble spread shows differences in both the magnitude and sign direction of the bias. For the Bias_run and Optimized_run, different ensembles from CESM2, CanESM5 and MPI show positive or negative bias in 2022 (**Figs. 2**, **S4**).

Here we reconstruct $spCO_2$ using only the pCO_2-Residual method. The testbed study by Hauck et al. (2023) used two different reconstruction methods; the MPI-SOM-FFN (Landschützer et al., 2023) and the Jena-MLS (Rödenbeck et al., 2015). In their sub-sampling experiments, assuming SOCAT coverage only, both methods underestimate $spCO_2$ leading to significant negative biases since year 2000. However, the underestimation was more significant for MPI-SOM-FFN, with negative biases generally > 5 µatm compared to < 5 µatm for Jena-MLS. This suggests that, at least the magnitude of bias, can be partly related to the mapping method itself. In their study, a single GOBM (i.e., FESOM-REcoM) was used as a testbed. These two reconstructions agree with some of our testbed ensembles in terms of negative biases over 2000-2015 (**Figs. 1**, **S4**) but are opposite of our 'testbed mean' (**Fig. 4**). Combined, current sub-sampling experiments suggest that the type of reconstruction method and ESM model structure impact the magnitude of bias and that the type of testbed model used (both GOBM or ESM) may impact the sign direction of bias.

5 Conclusions

We have demonstrated that switching the basis for hyperparameter selection from nMSE to bias when using the pCO_2-Residual method can improve reconstruction skill. When applied to actual SOCAT data, this leads to a significantly weaker global ocean carbon sink in 2022 (by ~ 0.5 Pg C/yr), and less of a divergence from GOBM estimates included in the GCB. This suggests that the increasingly stronger sink estimated by the pCO_2-Residual method, and potentially other reconstruction methods, might not represent real changes in the ocean. When using optimized hyperparameters, the reconstruction still leads to 'testbed mean' global reconstruction biases ±1 µatm over 1990-2022, and much larger biases regionally, especially in the Southern Ocean. Thus, as has also been shown in previous sub-sampling studies using a range of reconstruction methods and testbed structures (Bushinsky et al., 2019; Gloege et al., 2021; Djeutchouang et al., 2022; Hauck et al., 2023; Heimdal et al., 2024; Heimdal & McKinley, 2024), expanding the observational coverage of $spCO_2$, especially in the Southern Ocean, could further reduce reconstruction biases and improve our current estimates of ocean carbon uptake. Combining algorithmic bias corrections with targeted sampling in undersampled areas could be a promising path forward to reduce uncertainties of the ocean carbon sink.

Code availability

Data analysis scripts and supporting files are publicly available at https://github.com/OceanCarbon-LDEO-Columbia/pCO2Residual_Testbed.

Data availability

This publication uses the Pangeo-ESGF CMIP6 Zarr Data 2 (Busecke and Stern, 2024).

Author contribution

THH, GAM, APS and VA designed the experiments, and THH and APS performed the runs. THH, APS, DS and JB developed code. THH and ARF calculated air-sea fluxes. THH prepared the manuscript with contributions from all co-authors.

Competing interests

The authors declare that they have no conflict of interest.

Acknowledgements

We acknowledge funding from NOAA (Award #NA20OAR4310340), the European Space Agency via subaward from University of Exeter and NSF through the OCE Award #2333608 and the LEAP STC Award #2019625. We acknowledge the computing and storage resources provided by LEAP. VA acknowledges support from a PIVOT fellowship grant of the Simons Foundation (Award #981849). The authors acknowledge the World Climate Research Programme, which, through its Working Group on Coupled Modelling, coordinated and promoted CMIP6. The authors thank the climate modeling groups for producing and making available their model output, the Earth System Grid Federation (ESGF) for archiving the data and providing access, and the multiple funding agencies who support CMIP6 and ESGF. We thank Val Bennington for technical support.

References

Acquaviva, V., Barnes, E. A., Gagne, D. J., McKinley, G. A., and Thais, S.: Ethics in climate AI: From theory to practice, PLOS Climate, 3(8): e0000465, https://doi.org/10.1371/journal.pclm.0000465, 2024.

Acquaviva, V.: Machine learning for physics and astronomy, Princeton University Press, 2023.

Atlas, R., Hoffman, R. N., Ardizzone, J., Leidner, S. M., Jusem, J.C., Smith, D. K., and Gombos, D.: A cross-calibrated, multiplatform ocean surface wind velocity product for meteorological and oceanographic applications, Bulletin of the American Meteorological Society, 92, 157– 174, https://doi.org/10.1175/2010BAMS2946.1, 2011.

Bakker, D. C. E., Pfeil, B., Landa, C. S., Metzl, N., O'Brien, K. M., Olsen, A., Smith, K., Cosca, C., Harasawa, S., Jones, S. D., Nakaoka, S., Nojiri, Y., Schuster, U., Steinhoff, T., Sweeney, C., Takahashi, T., Tilbrook, B., Wada, C., Wanninkhof, R., Alin, S. R., Balestrini, C. F., Barbero, L., Bates, N. R., Bianchi, A. A., Bonou, F., Boutin, J., Bozec, Y., Burger, E. F., Cai, W.-J., Castle, R. D., Chen, L., Chierici, M., Currie, K., Evans, W., Featherstone, C., Feely, R. A., Fransson, A., Goyet, C., Greenwood, N., Gregor, L., Hankin, S., Hardman-Mountford, N. J., Harlay, J., Hauck, J., Hoppema, M., Humphreys, M. P., Hunt, C. W., Huss, B., Ibánhez, J. S. P., Johannessen, T., Keeling, R., Kitidis, V., Körtzinger, A., Kozyr, A., Krasakopoulou, E., Kuwata, A., Landschützer, P., Lauvset, S. K., Lefèvre, N., Lo Monaco, C., Manke, A., Mathis, J. T., Merlivat, L., Millero, F. J., Monteiro, P. M. S., Munro, D. R., Murata, A., Newberger, T., Omar, A. M., Ono, T., Paterson, K., Pearce, D., Pierrot, D., Robbins, L. L., Saito, S., Salisbury, J., Schlitzer, R., Schneider, B., Schweitzer, R., Sieger, R., Skjelvan, I., Sullivan, K. F., Sutherland, S. C., Sutton, A. J., Tadokoro, K., Telszewski, M., Tuma, M., van Heuven, S. M. A. C., Vandemark, D., Ward, B., Watson, A. J., and Xu, S.: A multi-decade record of high-quality fCO_2 data in version 3 of the Surface Ocean CO_2 Atlas (SOCAT), Earth System Science Data, 8, 383–413, https://doi.org/10.5194/essd-8-383-2016, 2016.

Bakker, D. C. E., Alin, S. R., Bates, N, Becker, M, Feely, R. A., Gkritzalis, T, Jones, S. D., Kozyr, A., Lauvset, S. K., Metzl, N., Munro, D. R., Nakaoka, S., Nojiri, Y., O'Brien, K. M., Olsen, A., Pierrot, D., Rehder, G., Steinhoff, T., Sutton, A. J., Sweeney, C., Tilbrook, B., Wada, C., Wanninkhof, R., Akl, J., Barbero, L., Beatty, C. M., Berghoff, C. F., Bittig, H. C., Bott, R., Burger, E. F., Cai, W., Castaño-Primo, R., Corredor, J. E., Cronin, M., De Carlo, E. H., DeGrandpre, M.D., Dietrich, C., Drennan, W. M., Emerson, S. R., Enochs, I. C., Enyo, K., Epherra, L., Evans, W., Fiedler, B., Fontela, M., Frangoulis, C., Gehrung, M., Giannoudi, L., Glockzin, M., Hales, B., Howden, S. D., Ibánhez, J. S. P., Kamb, L., Körtzinger, A., Lefèvre, N., Lo Monaco, C., Lutz, V. A., Macovei, V. A., Maenner Jones, S., Manalang, D., Manzello, D. P., Metzl, N., Mickett, J., Millero, F. J., Monacci, N. M., Morell, J. M., Musielewicz, S., Neill, C., Newberger, T., Newton, J., Noakes, S., Ólafsdóttir, S. R., Ono, T., Osborne, J., Padín, X. A., Paulsen, M., Perivoliotis, L., Petersen, W., Petihakis, G., Plueddemann, A. J., Rodriguez, C., Rutgersson, A., Sabine, C. L., Salisbury, J. E., Schlitzer, R., Skjelvan, I., Stamataki, N., Sullivan, K.F., Sutherland, S.C., T'Jampens, M., Tadokoro, K., Tanhua, T., Telszewski, M., Theetaert, H., Tomlinson, M., Vandemark, D., Velo, A., Voynova, Y. G., Weller, R. A., Whitehead, C., Wimart-Rousseau, C.: Surface Ocean CO_2 Atlas Database Version 2023 (SOCATv2023) (NCEI Accession 0278913), NOAA National Centers for Environmental Information [dataset], https://doi.org/10.25921/r7xa-bt92, 2023.

Bennington, V., Galjanic, T., and McKinley, G. A.: Explicit Physical Knowledge in Machine Learning for Ocean Carbon Flux Reconstruction: The pCO_2-Residual Method, Journal of Advances in Modeling Earth Systems, 14(10), https://doi.org/10.1029/2021ms002960, 2022a.

Bennington, V., Gloege, L., and McKinley, G. A.: Variability in the global ocean carbon sink from 1959 to 2020 by correcting models with observations, Geophysical Research Letters, 49(14), https://doi.org/10.1029/2022GL098632, 2022b.

Busecke, J. J. M., and Stern, C. I.: cmip6-leap-feedstock (v0.2.0), Zenodo, https://doi.org/10.5281/zenodo.10621538, 2024.

Bushinsky, S. M., Landschützer, P., Rödenbeck, C., Gray, A. R., Baker, D., Mazloff, M. R., Resplandy, L., Johnson, K. S., and Sarmiento, J. L.: Reassessing Southern Ocean air-sea CO_2 flux estimates with the addition of biogeochemical float observations, Global Biogeochemical Cycles, *33*(11), 1370-1388, https://doi.org/10.1029/2019GB006176, 2019.

Chen, T., and Guestrin, C.: Xgboost: A scalable tree boosting system, In: Proceedings of the 22nd ACM SIGKDD international conference on knowledge discovery and data mining (pp. 785-794), https://doi.org/10.1145/2939672.2939785, 2016.

Denvil-Sommer, A., Gehlen, M., and Vrac, M.: Observation system simulation experiments in the Atlantic Ocean for enhanced surface ocean pCO_2 reconstructions, Ocean Science, 17, 1011-1030, https://doi.org/10.5194/os-17-1011-2021, 2021.

Djeutchouang, L. M., Chang, N., Gregor, L., Vichi, M., and Monteiro, P. M. S.: The sensitivity of pCO_2 reconstructions to sampling scales across a Southern Ocean sub-domain: a semi-idealized ocean sampling simulation approach, Biogeosciences, 19, 4171-4195, https://doi.org/10.5194/bg-19-4171-2022, 2022.

Dong, Y., Bakker, D. C. E., and Landschützer, P.: Accuracy of ocean CO_2 uptake estimates at risk by a reduction in the data collection, Geophysical Research Letters, 51(9), e2024GL108502, https://doi.org/10.1029/2024GL108502, 2024a.

Dong, Y., Bakker, D. C. E., Bell, T. G., Yang, M., Landschützer, P., Hauck, J., Rödenbeck, C., Kitidis, V., Bushinsky, S. M., and Luss, P. S.: Direct observational evidence of strong CO_2 uptake in the Southern Ocean, Science Advances, 10, eadn5781, DOI: 10.1126/sciadv.adn5781, 2024b.

Fay, A. R., Gregor, L., Landschützer, P., McKinley, G. A., Gruber, N., Gehlen, M., Iida, Y., Laruelle, G. G., Rödenbeck, C., Roobaert, A., and Zeng, J.: SeaFlux: harmonization of air-sea CO_2 fluxes from surface pCO_2 data products using a standardized approach, Earth System Science Data, 13, 4693-4710, https://doi.org/10.5194/essd-13-4693-2021, 2021.

Friedlingstein, P., O'Sullivan, M., Jones, M. W., Andrew, R. M., Bakker, D. C. E., Hauck, J., Landschützer, P., Le Quéré, C., Luijkx, I. T., Peters, G. P., Peters, W., Pongratz, J., Schwingshackl, C., Sitch, S., Canadell, J. G., Ciais, P., Jackson, R. B., Alin, S. R., Anthoni, P., Barbero, L., Bates, N. R., Becker, M., Bellouin, N., Decharme, B., Bopp, L., Brasika, I. B. M., Cadule, P., Chamberlain, M. A., Chandra, N., Chau, T.-T.-T., Chevallier, F., Chini, L. P., Cronin, M., Dou, X., Enyo, K., Evans, W., Falk, S., Feely, R. A., Feng, L., Ford, D. J., Gasser, T., Ghattas, J., Gkritzalis, T., Grassi, G., Gregor, L., Gruber, N., Gürses, Ö., Harris, I., Hefner, M., Heinke, J., Houghton, R. A., Hurtt, G. C., Iida, Y., Ilyina, T., Jacobson, A. R., Jain, A., Jarníková, T., Jersild, A., Jiang, F., Jin, Z., Joos, F., Kato, E., Keeling, R. F., Kennedy, D., Klein Goldewijk, K., Knauer, J., Korsbakken, J. I., Körtzinger, A., Lan, X., Lefèvre, N., Li, H., Liu, J., Liu, Z., Ma, L., Marland, G., Mayot, N., McGuire, P. C., McKinley, G. A., Meyer, G., Morgan, E. J., Munro, D. R., Nakaoka, S.-I., Niwa, Y., O'Brien, K. M., Olsen, A., Omar, A. M., Ono, T., Paulsen, M., Pierrot, D., Pocock, K., Poulter, B., Powis, C. M., Rehder, G., Resplandy, L., Robertson, E., Rödenbeck, C., Rosan, T. M., Schwinger, J., Séférian, R., Smallman, T. L., Smith, S. M., Sospedra-Alfonso, R., Sun, Q., Sutton, A. J., Sweeney, C., Takao, S., Tans, P. P., Tian, H., Tilbrook, B., Tsujino, H., Tubiello, F., van der Werf, G. R., van Ooijen, E., Wanninkhof, R., Watanabe, M., Wimart-Rousseau, C., Yang, D., Yang, X., Yuan, W., Yue, X., Zaehle, S., Zeng, J., and Zheng, B.: Global Carbon Budget 2023, Earth System Science Data, 15, 5301–5369, https://doi.org/10.5194/essd-15-5301-2023, 2023.

Gloege, L., McKinley, G. A., Landschützer, P., Fay, A. R., Frolicher, T. L., and Fyfe, J. C.: Quantifying Errors in Observationally Based Estimates of Ocean Carbon Sink Variability, Global Biogeochemical Cycles, 35(4), https://doi.org/10.1029/2020gb006788, 2021.

Gloege, L., Yan, M., Zheng, T. and McKinley, G. A.: Improved quantification of ocean carbon uptake by using machine learning to merge global models and pCO_2 data, Journal of Advances in Modeling Earth Systems, 14(2), https://doi.org/10.1029/2021MS002620, 2022.

Good, S. A., Martin, M. J., and Rayner, N. A.: EN4: Quality controlled ocean temperature and salinity profiles and monthly objective analyses with uncertainty estimates, Journal of Geophysical Research: Oceans, 118, 6704–6716, https://doi.org/10.1002/2013JC009067, 2013.

Gregor, L. and Fay, A. R.: Air-sea CO_2 fluxes for surface pCO_2 data products using a standardized approach, Zenodo [code], https://doi.org/10.5281/zenodo.8280457, 2021.

Gregor, L., Lebehot, A. D., Kok, S., and Scheel Monteiro, P. M.: A comparative assessment of the uncertainties of global surface ocean CO_2 estimates using a machine-learning ensemble (CSIR-ML6 version 2019a) – have we hit the wall? Geoscientific Model Development, 12(12), 5113–5136, https://doi.org/10.5194/gmd-12-5113-2019, 2019.

Hauck, J., Nissen, C., Landschützer, P., Rödenbeck, C., Bushinsky, S., and Olsen, A.: Sparse observations induce large biases in estimates of the global ocean CO2 sink: and ocean model sub-sampling experiment, Philosophical Transactions Of the Royal Society A, 381:20220063, https://doi.org/10.1098/rsta.2022.0063, 2023.

Heimdal, T. H., McKinley, G. A., Sutton, A. J., Fay, A. R., and Gloege, L.: Assessing improvements in global ocean pCO_2 machine learning reconstructions with Southern Ocean autonomous sampling, Biogeosciences, 21, 2159-2176, https://doi.org/10.5194/bg-21-2159-2024, 2024.

Heimdal, T. H., and McKinley, G. A.: Using observing system simulation experiments to assess impacts of observational uncertainties in surface ocean pCO_2 machine learning reconstructions, Scientific Reports, 14, 19763, https://doi.org/10.1038/s41598-024-70617-x.

Hersbach, H., Bell, B., Berrisford, P., Hirahara, S., Horányi, A., Muñoz-Sabater, J., Nicolas, J., Peubey, C., Radu, R., Schepers, D., Simmons, A., Soci, C., Abdalla, S., Abellan, X., Balsamo, G., Bechtold, P., Biavati, G., Bidlot, J., Bonavita, M., De Chiara, G., Dahlgren, P., Dee, D., Diamantakis, M., Dragani, R., Flemming, J., Forbes, R., Fuentes, M., Geer, A., Haimberger, L., Healy, S., Hogan, R.J., Hólm, E., Janisková, M., Keeley, S., Laloyaux, P., Lopez, P., Lupu, C., Radnoti, G., de Rosnay, P., Rozum, I., Vamborg, F., Villaume, S., and Thépaut, J.: The ERA5 global reanalysis, Quarterly Journal of the Royal Meteorological Society, 146, 1999–2049, https://doi.org/10.1002/qj.3803, 2020 (data available at: https://cds.climate.copernicus.eu/cdsapp#!/dataset/reanalysis-era5-single-levels-monthly-means?tab=overview).

Jersild, A., and Landschützer, P.: A spatially explicit uncertainty analysis of the air-sea CO_2 flux from observations, Geophysical Research Letters, 51(4), e2023GL106636, https://doi.org/10.1029/2023GL106636, 2024.

Khatiwala, S., Primeau, F., and Hall., T.: Reconstruction of the history of anthropogenic CO2 concentrations in the ocean, Nature, 462(7271), 346-349, https://doi.org/10.1038/nature08526, 2009.

Kobayashi, S., Ota, Y., Harada, Y., Ebita, A., Moriya, M., Onoda, H., Onogi, K., Kamahori, H., Kobayashi, C., Endo, H., Miyaoka, K., and Takahashi, K.: The JRA-55 Reanalysis: General Specifications and Basic Characteristics, Journal of the Meteorological Society of Japan, 93, 5–48, https://doi.org/10.2151/jmsj.2015-001, 2015.

Landschützer, P., Gruber, N., Bakker, D. C. E., and Schuster, U.: Recent variability of the global ocean carbon sink, Global Biogeochemical Cycles, 28(9), 927-949, https://doi.org/10.1002/2014GB004853, 2014.

Landschützer, P., Tanhua, T., Behncke, J., and Keppler, L.: Sailing through the Southern Ocean seas of air-sea CO_2 flux uncertainty, Philosophical Transactions of the Royal Society A, 381, https://doi.org/10.1098/rsta.2022.0064, 2023.

Long, M. C., Stephens, B. B., McKain, K., Sweeney, C., Keeling, R. F., Kort, E. A., Morgan, E. J., Bent, J. D., Chandra, N., Chevallier, F., Commane, R., Daube, B. C., Krummel, P. B., Loh, Z., Luijkx, I. T., Munro, D., Patra, P., Peters, W., Ramonet, M., Rödenbeck, C., Stavert, A., Tans, P., and Wofsy, S. C.: Strong Southern Ocean carbon uptake evident in airborne observations, Science, 374(6572), 1275-1280, https://doi.org/10.1126/science.abi4355, 2021.

Mackay, N., Watson, A., Suntharalingam, P., Chen, Z., and Rödenbeck, C.: Improved winter data coverage of the Southern Ocean CO_2 sink from extrapolation of summertime observations, Communications Earth & Environment, 3, 265, https://doi.org/10.1038/s43247-022-00592-6, 2022.

Nickford, S., Palter, J. B., and Mu, L.: The importance of contemporaneous wind and pCO_2 measurements for regional air-sea CO_2 flux estimates, Journal of Geophysical Research: Oceans, 129, e2023JC020744, https://doi.org/10.1029/2023JC020744, 2024.

Eyring, V., Bony, S., Meehl, G. A., Senior, C. A., Stevens, B., Stouffer, R. J., and Taylor, K. E.: Overview of the Coupled Model Intercomparison Project Phase 6 (CMIP6) experimental design and organization, Geoscientific Model Development, 9, 1937-1958, https://doi.org/10.5194/gmd-9-1937-2016, 2016.

Reynolds, R. W., Rayner, N. A., Smith, T. M., Stokes, D. C., and Wang, W.: An improved in situ and satellite SST analysis for climate, Journal of Climate, 15, 1609–1625, https://doi.org/10.1175/1520-0442(2002)015<1609:AIISAS>2.0.CO;2, 2002 (data available at: https://psl.noaa.gov/data/gridded/data.noaa.oisst.v2.html).

Roobaert, A., Laruelle, G. G., Landschützer, P., and Regnier, P.: Uncertainty in the global oceanic CO_2 uptake induced by wind forcing: quantification and spatial analysis, Biogeosciences, 15(6), 1701-1720, https://doi.org/10.5194/bg-15-1701-2018, 2018.

Rödenbeck, C., Bakker, D. C. E., Gruber, N., Iida, Y., Jacobson, A. R., Jones, S., Landschützer, P., Metzl, N., Nakaoka, S., Olsen, A., Park, G.-H., Peylin, P., Rodgers, K. B., Sasse T. P., Schuster, U., Shutler, J. D., Valsala, V., Wannikkhof, R., and Zeng, J.: Data-based estimates of the ocean carbon sink variability – first results of the Surface Ocean pCO_2 Mapping intercomparison (SOCOM), Biogeosciences, 12, 7251-7278, https://doi.org/10.5194/bg-12-7251-2015, 2015.

Rödenbeck, C., DeVries, T., Hauck, J., Le Quéré, C., Keeling, R. F.: Data-based estimates of interannual sea-air CO_2 flux variations 1957-2020 and their relation to environmental drivers, Biogeosciences, 19, 2627-2652, https://doi.org/10.5194/bg-19-2627-2022, 2022.

Stamell, J., Rustagi, R. R., Gloege, L., and McKinley, G. A.: Strengths and weaknesses of three Machine Learning methods for pCO_2 interpolation, Geoscientific Model Development Discussions[preprint], doi:10.5194/gmd-2020-311, 22 October 2020.

Sutton, A. J., Williams, N. L., and Tilbrook, B.: Constraining Southern Ocean CO_2 flux uncertainty using uncrewed surface vehicle observations, Geophysical Research Letters, 48(3), e2020GL091748, https://doi.org/10.1029/2020GL091748, 2021.

Takahashi, T., Sutherland, S. C., Sweeney, C., Poisson, A., Metzl, N., Tilbrook, B., Bates, N. R., Wanninkhof, R., Feely, R. A., Sabine, C., Olafsson, J., and Nojiri, Y.: Global sea-air CO_2 flux based on climatological surface ocean pCO_2, and seasonal biological and temperature effects, Deep Sea Research Part II: Topical Studies in Oceanography, 49(9-10), 1601-1622, https://doi.org/10.1016/S0967-0645(02)00003-6, 2002.

Watson, A. J., Schuster, U., Shutler, J. D., Holding, T., Ashton, I. G. C, Landschützer, P., Woolf, a. K., and Goddijn-Murphy, L.: Revised estimates of ocean-atmosphere CO2 flux are consistent with ocean carbon inventory, Scientific Reports, 11, 4422, https://doi.org/10.1038/s41467-020-18203-3, 2020.

Zhong, G., Li, X., Song, J., Wang, F., Qu, B., Wang, Y., Zhang, B., Ma, J., Yuan, H., Duan, L., Wang, Q., Xing, J., and Dai., J.: The Southern Ocean carbon sink has been overestimated in the past three decades, Communications Earth & Environment, 5, 398, https://doi.org/10.1038/s43247-024-01566-6, 2024.

Supplementary Material

S1. Supplementary Text – The shuffled runs

To test if the trend of increasingly negative 2017-2022 reconstruction bias is a result of declining SOCAT coverage, we shuffled the years of the original SOCATv2023 (Bakker et al., 2023) sampling mask five times and reconstructed $spCO_2$ for one member per ESM (nine in total), using identical hyperparameters as those of the nMSE_run (**Table 4**). The original SOCAT distribution shows consistently sparse observations in the 1980s, before a steady increase occur in the 1990s until 2017 (**Fig. S1**). From 2017 until 2022, the observations decrease. The five shuffled masks are created using the same sampling patterns as in the original SOCAT, but randomly changing the year of that sampling between 1982 and 2022 (**Fig. S1**).

We calculated the mean $spCO_2$ value and year from the testbed (mean of 9 members) based on each sampling mask. The mean $spCO_2$ for the original mask is 370 µatm and occur in 2012, while the $spCO_2$ means for the five shuffled mask range from 355 µatm and 360 µatm and occurs in years 2002-2006. The mean $spCO_2$ of the full testbed (considering all 1 °x1° grid cells, no mask applied) is 356 µatm and occurs in 2002. We calculated annual global mean reconstruction biases (absolute values) for each reconstruction, and compared the biases to the number of monthly 1°x1° SOCAT observations per year for all years between 1982 and 2022 for all masks (**Fig. S2**). There is no correlation between the annual mean biases (see also **Fig. 3**) and number of SOCAT observations in that year.

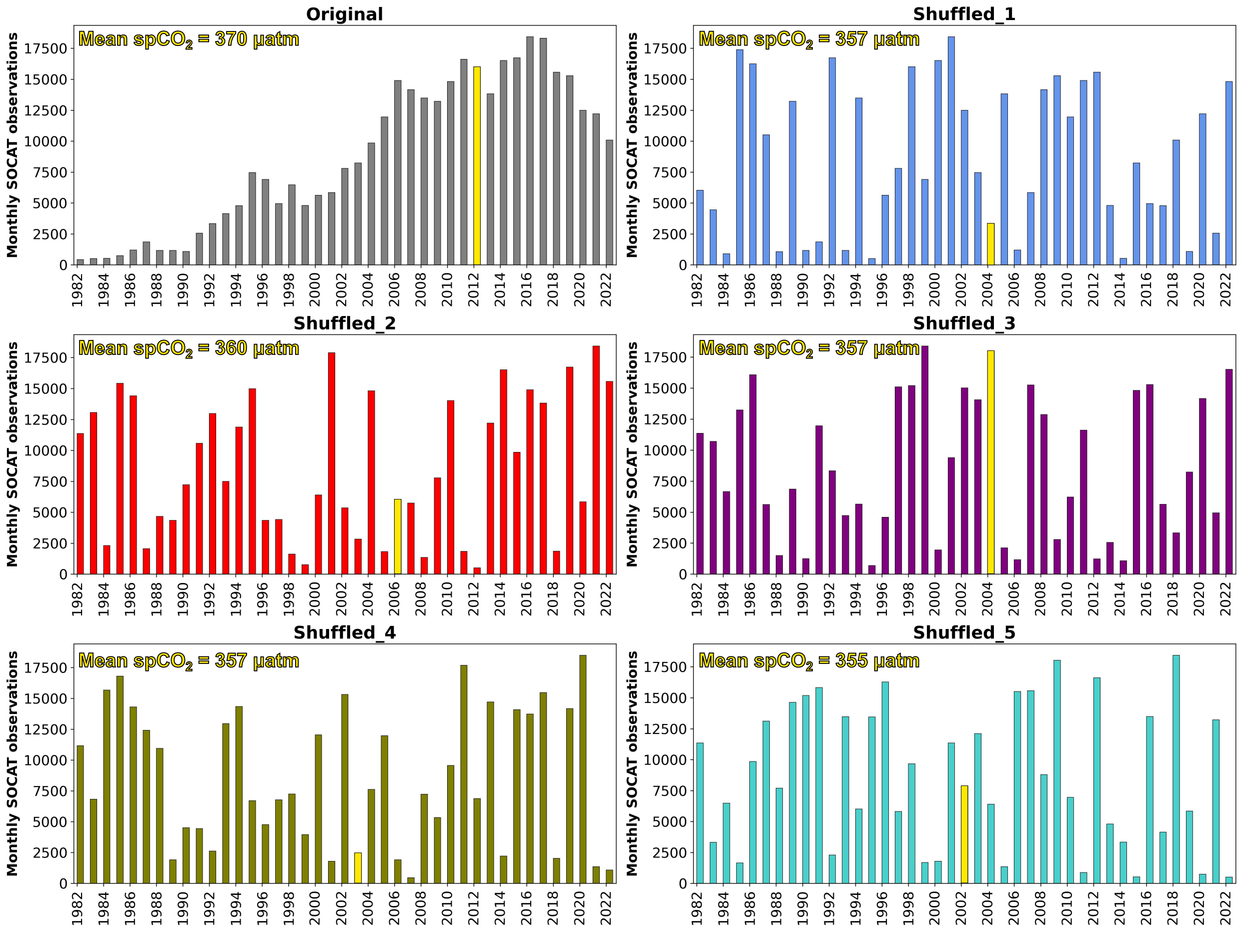

Figure S1: Number of monthly 1°x1° SOCAT observations annually from 1982-2022 for six different SOCAT sampling masks. Original (gray bars) = SOCATv2023 (Bakker et al., 2023). Shuffled_1-5 (colored bars) = years of the original SOCAT mask randomly shuffled. Yellow bars in each panel represent the year corresponding to the mean 'testbed truth' $spCO_2$ for each sampling mask.

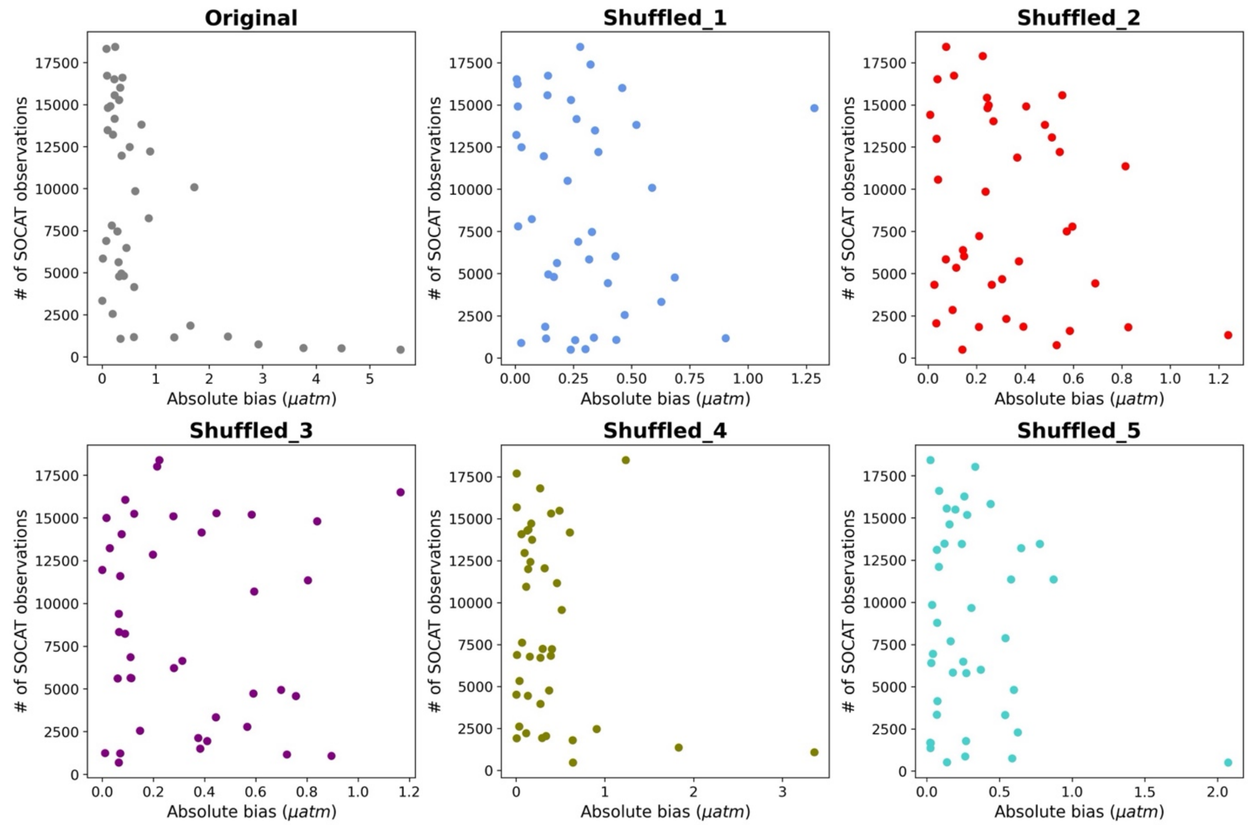

Figure S2: Correlation of monthly 1°x1° SOCAT observations and annual global mean reconstruction absolute bias for all years between 1982 and 2022. Original (gray dots) = reconstructions using the original SOCAT mask (v2023; Bakker et al., 2023). Shuffled_1-5 (colored dots) = reconstructions using the shuffled SOCAT masks.

S2. Supplementary Text – The optimized run

We explore if it is possible to further improve reconstruction bias beyond using bias as error metric during hyperparameter selection for each ESM. We performed additional reconstructions (the Optimized_run) where we applied the combination of hyperparameters that led to reconstruction biases closest to zero throughout the whole testbed period. This combination corresponds to that chosen for the Bias_run sub-sampling CESM2-WACCM (**Fig. 1**; **Table 5**). These optimized hyperparameters (maximum depth level: 6; learning rate: 0.3; decision trees: 4,000; **Table 4**) were applied to all 45 members of the testbed.

When using the optimized hyperparameters, the 'testbed mean' shows that the tendency to overestimate $spCO_2$ in the 1980s, and underestimate $spCO_2$ over 2017-2022 is significantly reduced compared to the nMSE_run and the Bias_run (**Fig. 4**). 2017-2022 ESM mean reconstruction biases are similar or closer to zero compared to those of the Bias_run, and most 2017-2022 ESM mean reconstruction RMSEs are lower (**Table S1**). Negative ESM mean reconstruction biases over 2017-2022 are only shown for CMCC, CanESM5 and MPI (**Table S1)**. Considering the whole testbed period, annual global ESM mean reconstruction biases for the Optimized_run and the Bias_run are very similar; notably better performance is only shown for ACCESS, CMCC and UKESM1 in the 1980s, and for CMCC and UKESM1 in the last years of the testbed (**Fig. S3**). **Figure S4** shows the ensemble spread; generally, positive bias over 2017-2022 is shown for most members of ACCESS, CESM2, CESM2-WACCM and GFDL, and negative bias for members of CMCC and MPI. For CanESM5, MPI and UKESM1 there is a larger spread, but these ESMs also have more members.

ESM name (# of members)	nMSE_run | Bias_run | Optimized_run **BIAS**	**RMSE**
UKESM1-0-LL (5)	-0.7 | -0.7 | 0.2	10.2 | 10.4 | 10.1
ACCESS-ESM1-5 (2)	-0.01 | 0.4 | 0.5	10.7 | 10.7 | 10.4
CMCC-ESM2 (1)	-1.1 | -1.3| -0.5	10.8 | 12.5 | 10.6
CESM2-WACCM (3)	-0.7 | 0.08 | 0.08	9.2 | 9.1 | 9.1
CESM2 (3)	-0.4 | 0.4 | 0.4	9.2 | 8.4 | 9.0
CanESM5-CanOE (3)	-0.2 | 0.08 | 0.03	8.9 | 9.5 | 9.3
CanESM5 (18)	-0.3 | -0.3 | -0.2	8.8 | 8.8 | 9.3
MPI-ESM1-2-LR (9)	-1.5 | -0.5 | -0.6	12.9 | 13.6 | 13.0
GFDL-ESM4 (1)	-0.9 | 0.1 | 0.2	11.2 | 11.6 | 10.9
Testbed mean	**-0.6 | -0.2 | 0.00**	**10.2 | 10.5 | 10.2**

Table S1: Global 2017-2022 mean reconstruction bias and RMSE for individual ESMs sub-sampled (ESM mean) and the 'testbed mean'.

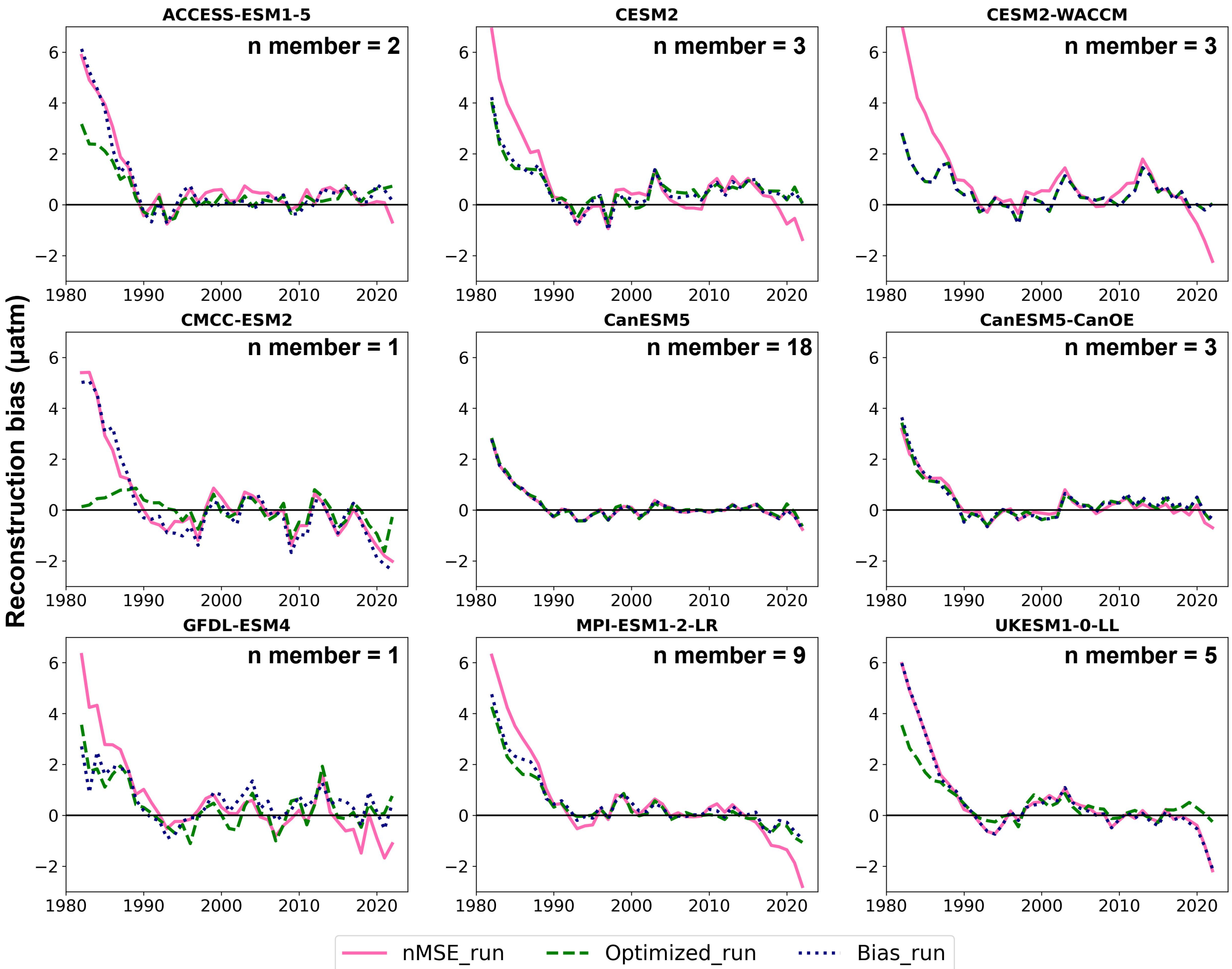

Figure S3: Annual global ESM mean reconstruction bias for the nMSE_run (pink solid), Bias_run (blue dotted) and Optimized_run (green dashed). nMSE_run = hyperparameters were chosen based on negative mean squared error (nMSE) as error metric. Bias_run = hyperparameters were chosen based on bias as error metric. Optimized_run = all runs used a set of optimized hyperparameters (depth level: 6; learning rate: 0.3; decision trees: 4,000).

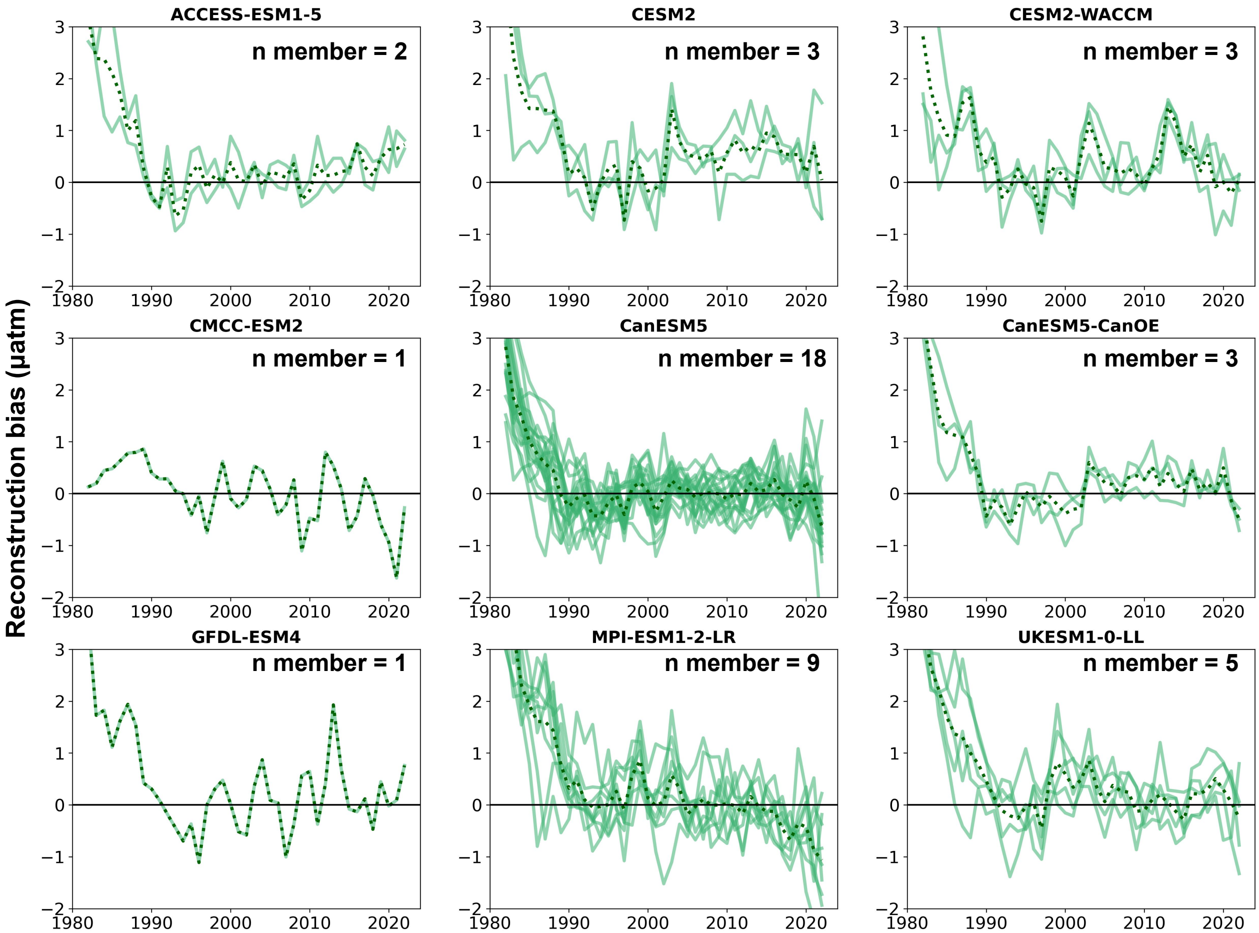

Figure S4: Annual global mean reconstruction bias for the 45 reconstructions of the testbed for the Optimized_run, grouped by ESM. Bold dotted lines are ESM means.

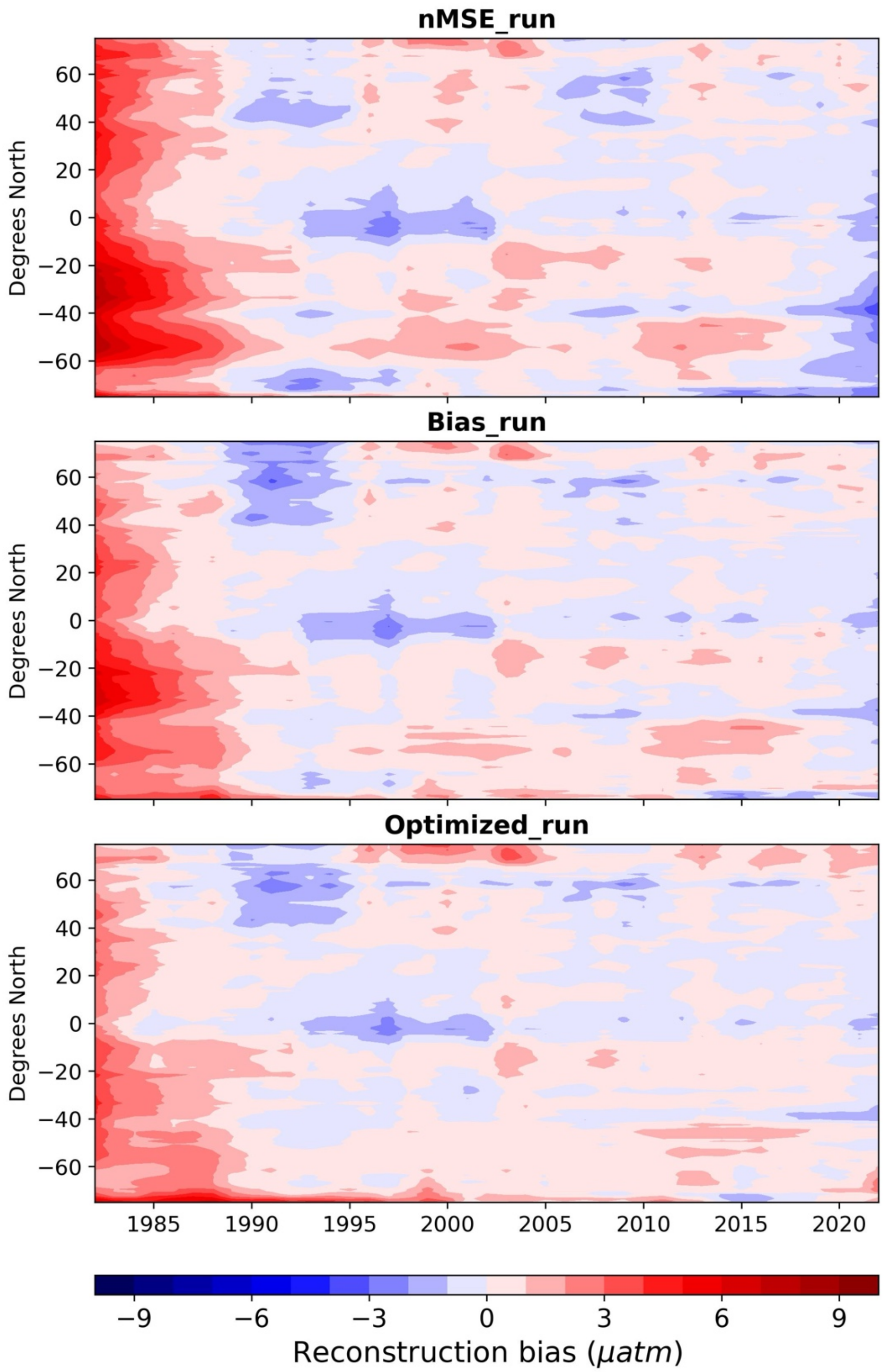

Figure S5: Zonal mean, annual mean Hovmöller of reconstruction bias (‘testbed mean’; 45 members) for the nMSE_run, Bias_run and the Optimized_run.

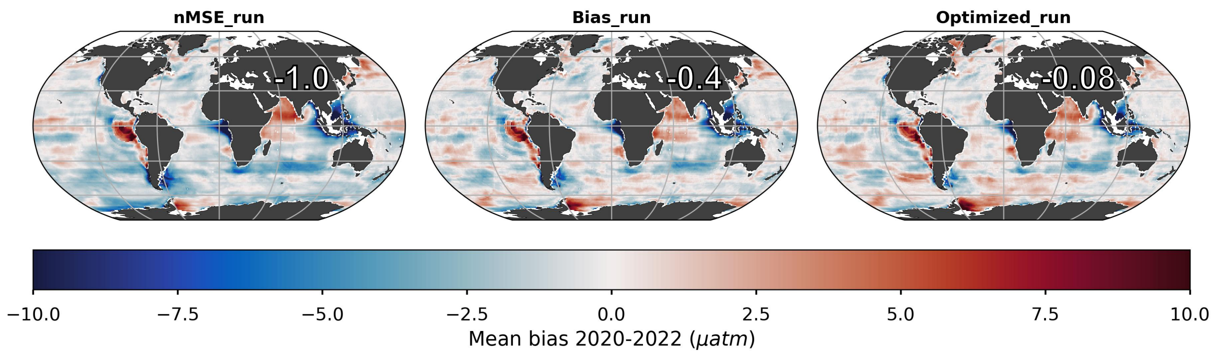

Figure S6: Mean 2020-2022 reconstruction bias ('testbed mean'; 45 members) for the nMSE_run, Bias_run and Optimized_run. Values on panels show the global mean (2020-2022) bias in µatm.

Test error metrics	Optimized | Original					
Mean (1982-2022)	**Run 1**	**Run 2**	**Run 3**	**Run 4**	**Run 5**	**Mean**
RMSE (uatm)	18.5 | 18.8	18.5 | 18.7	19.2 | 19.4	19 | 19.4	18.6 | 18.7	**18.8 | 19.0**
Bias (uatm)	0.3 | 0.4	-0.7 | -0.5	-0.1 | 0.1	-0.3 | -0.2	0.1 | -0.01	**-0.1 | -0.07**
Mean AE (uatm)	12.2 | 12.4	12.2 | 12.3	12.6 | 12.7	12.5 | 12.8	12.3 | 12.4	**12.4 | 12.5**
Median AE (uatm)	8.2 | 8.2	8.0 | 8.1	8.3 | 8.4	8.2 | 8.5	8.2 | 8.2	**8.2 | 8.3**
Correlation	0.91 | 0.90	0.91 | 0.90	0.90 | 0.90	0.90 | 0.90	0.91 | 0.91	**0.91 | 0.90**

Table S2: Test statistics (global mean over 1982-2022) for the fCO_2 reconstructions using real-world SOCAT data (SOCATv2023; Bakker et al., 2023). Optimized = reconstruction using the optimized hyperparameters from this study. Original = reconstruction using hyperparameters from Bennington et al. (2022a) based on nMSE as error metric during algorithm optimization. The machine learning model is run five times (Run 1-5).